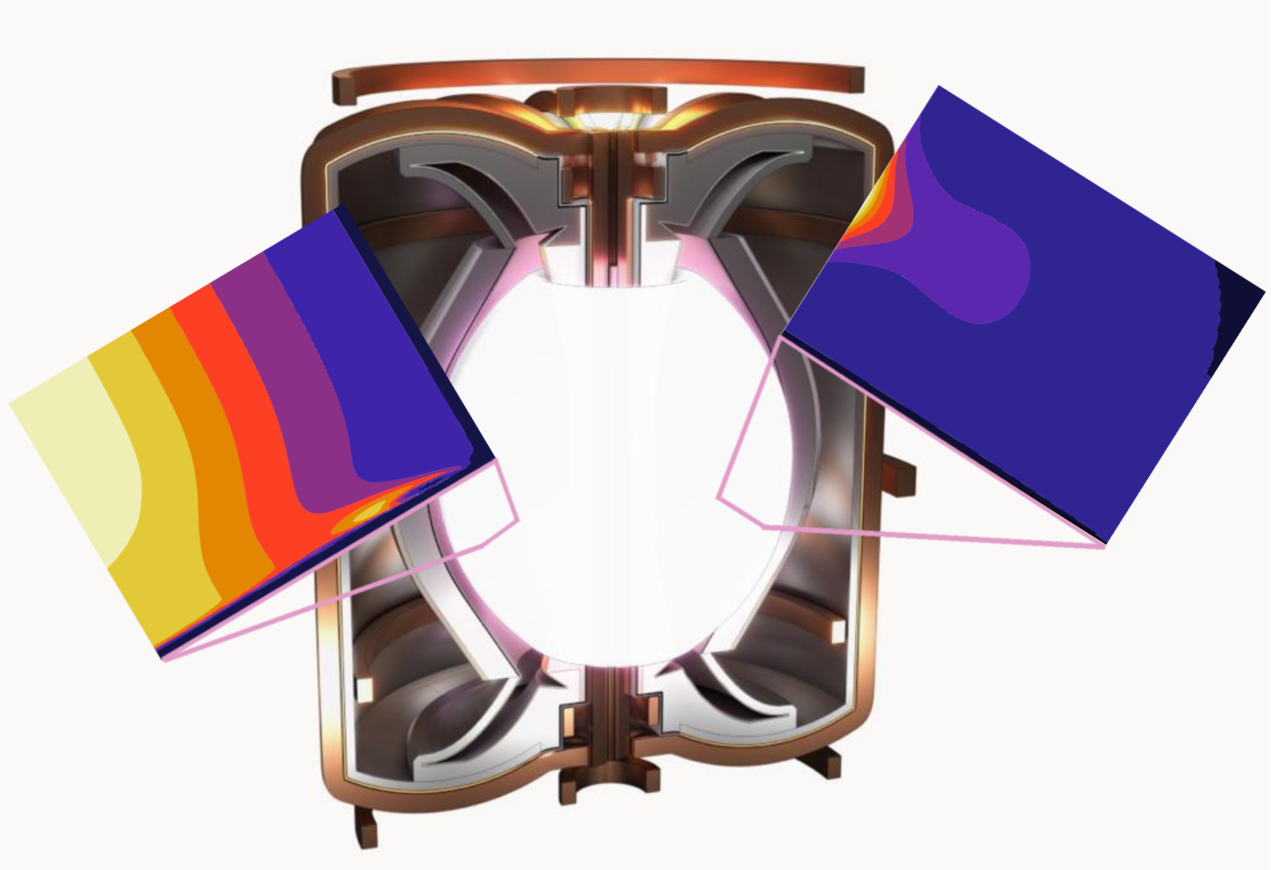

Runaway Dynamics in Reactor-Scale Spherical Tokamak Disruptions

Thesis for the degree of Master of Science in Physics

ESMÉE BERGER

DEPARTMENT OF PHYSICS
CHALMERS UNIVERSITY OF TECHNOLOGY
Gothenburg, Sweden 2022
www.chalmers.se

Thesis for the degree of Master of Science

Runaway Dynamics in Reactor-Scale Spherical Tokamak Disruptions

ESMÉE BERGER

Department of Physics
Division of Subatomic, High Energy and Plasma Physics
Plasma Theory Research Group
Chalmers University of Technology
Gothenburg, Sweden 2022

Runaway Dynamics in Reactor-Scale Spherical Tokamak Disruptions
ESMÉE BERGER

Supervisors: István Pusztai, Department of Physics
Sarah Newton, Department of Physics and
Culham Centre for Fusion Energy (UK)
Examiner: Tünde Fülöp, Department of Physics

Thesis for the degree of Master of Science
Department of Physics
Division of Subatomic, High Energy and Plasma Physics
Plasma Theory Research Group
Chalmers University of Technology
SE-412 96 Gothenburg
Telephone +46 31 772 1000

Cover: Illustration of a plasma in a spherical tokamak reactor concept design (STEP) together with the time evolution of the radial distribution of runaway generation rates for two different mechanisms, Dreicer (left, see Figure 4.3a) and avalanche (right, see Figure 4.3d), during a disruption simulated with DREAM.

Typeset in LaTeX
Printed by Chalmers Reproservice
Gothenburg, Sweden 2022

Runaway Dynamics in Reactor-Scale Spherical Tokamak Disruptions
ESMÉE BERGER
Department of Physics
Chalmers University of Technology

Abstract

One of the most promising concepts to achieve commercial fusion power, to date, is a toroidal magnetic confinement system centred around a *tokamak*. To aid the development, compact *spherical tokamaks* have long been proposed as component testing facilities. There is also an effort to design and construct spherical tokamaks suitable for energy production, with an example being the STEP program in the UK. One of the remaining obstacles for all reactor-scale tokamaks is so-called *runaway electrons* — electrons accelerated to relativistic speeds. These can be generated during *disruptions*, which are off-normal events where the confinement of the plasma is rapidly lost. As runaway electrons can severely damage the machine walls, their production and mitigation has been extensively studied for conventional tokamaks. However, due to the disruption dynamics typically being different in spherical tokamaks, the existing results cannot directly be transferred to these more compact devices. Therefore, runaway dynamics in reactor-scale spherical tokamaks is investigated in this work. We consider both the severity of runaway generation during unmitigated disruptions, as well as the effect that typical mitigation schemes based on massive material injection have on runaway production. The study is conducted using the numerical framework DREAM (*Disruption Runaway Electron Analysis Model*) and we find that, in many cases, mitigation strategies are necessary if the runaway current is to be prevented from reaching multi-megaampere levels. Our results indicate that with a suitably chosen deuterium-neon mixture for mitigation, it is possible to achieve a tolerable runaway current and ohmic current evolution. With such parameters, however, the majority of the thermal energy loss happens through radial transport rather than radiation, which poses a risk of unacceptable localised heat loads.

Keywords: fusion plasma, spherical tokamak, runaway electron, disruption mitigation, material injection

Acknowledgements

I am very grateful for having had the opportunity to work with the members of the Plasma Theory Research Group at Chalmers. I would like to especially thank my examiner Tünde for introducing me to the interesting field of magnetic fusion, for her relentless support, and for creating a great work environment. I would also like to express my sincerest gratitude to my supervisors, István and Sarah, for their endless help with any and all physics questions and their very valuable feedback on the thesis. A special thanks also to Mathias, for always being prepared to discuss my questions, be it about computational issues, runaway physics or general early scientific career things; to Oskar, for sharing his knowledge about previous related results for conventional tokamaks; to Andréas, for discussions ranging from general physics topics to very specific LaTeX issues; and to members of the STEP program, especially Alexandre who prepared the input data, for the collaboration.

Last but not least, I would like to thank my family and friends for their support and encouragement throughout.

Esmée Berger, Gothenburg, June 2022

List of Acronyms

Below is a list of acronyms that have been used throughout this thesis, in alphabetical order.

BurST	Burning Spherical Tokamak
CC	Current Conversion
CQ	Current Quench
DREAM	Disruption Runaway Electron Analysis Model
MCF	Magnetic Confinement Fusion
ST	Spherical Tokamak
STEP	Spherical Tokamak for Energy Production
TQ	Thermal Quench

Nomenclature

Below is a selection of symbols that have been used throughout this thesis, including their typical units.

a	Plasma minor radius [m]
b	Wall radius [m]
B_θ	Poloidal magnetic field component [T]
B_φ	Toroidal magnetic field component [T]
δ	Triangularity
Δ	Shafranov shift [m]
ϵ	Inverse aspect ratio
E_c	Critical electric field for runaway generation [V/m]
E_D	Dreicer field [V/m]
$E_\parallel$	Electric field component parallel to the magnetic field lines [V/m]
γ_Compton	Compton runaway rate [$\mathrm{s}^{-1}\mathrm{m}^{-3}$]
γ_Dreicer	Dreicer runaway rate [$\mathrm{s}^{-1}\mathrm{m}^{-3}$]
$\gamma_\text{hot-tail}$	Hot-tail runaway rate [$\mathrm{s}^{-1}\mathrm{m}^{-3}$]
γ_tritium	Tritium runaway rate [$\mathrm{s}^{-1}\mathrm{m}^{-3}$]
Γ_ava	Avalanche multiplication rate [s^{-1}]
G	Toroidal magnetic field function [T m]
I_ohm	Ohmic current [MA]
I_re	Runaway current [MA]
I_tot	Total plasma current [MA]
$I_\mathrm{tot,0}$	Initial plasma current [MA]
j	Total current density parallel to magnetic field lines [$\mathrm{MA/m}^2$]
j_0	Initial total current density parallel to magnetic field lines [$\mathrm{MA/m}^2$]
j_ohm	Ohmic current density parallel to magnetic field lines [$\mathrm{MA/m}^2$]
j_re	Runaway current density parallel to magnetic field lines [$\mathrm{MA/m}^2$]
κ	Elongation

m_e	Electron mass [kg]
n_e	Electron density [m^{-3}]
n_e0	Initial electron density [m^{-3}]
$n_i^{(j)}$	Ion density of species i with charge state j [m^{-3}]
n_re	Runaway electron density [m^{-3}]
ψ_ref	Reference poloidal flux [Wb]
r	Minor radius coordinate/flux surface label [m]
r_wall	Distance between plasma and wall [cm]
R	Major radius coordinate [m]
R_0	Major radius of the magnetic axis [m]
t_0	Thermal quench decay time scale [ms]
t_CQ	Current quench time [ms]
t_wall	Resistive timescale of the wall [ms]
T_0	Initial electron temperature [keV]
T_e	Electron temperature [eV]
T_f	Final electron temperature [eV]
v_c	Critical runaway speed parallel to the magnetic field lines [m/s]
$v_\parallel$	Velocity component parallel to the magnetic field lines [m/s]
$v_\mathrm{th,e}$	Thermal electron speed [m/s]
W_e	Thermal electron energy density [J/m^3]

Contents

1

Introduction

Imagine a future where there exists a sustainable energy source that lacks the intermittency of solar and wind power and provides the same energy density as nuclear fission, without producing any long-lived radioactive waste. Such an energy source would play an essential role in combating further global climate change while simultaneously catering to the steadily increasing energy demand. Nuclear fusion, where energy is released when two small nuclei fuse into a larger nucleus with lower mass than the total initial mass, offers this possibility (Freidberg, 2007).

Fusion is the power source of the stars, including our own: the Sun. Due to the high temperature, the constituents of stars are in the plasma state, meaning that the atoms are decomposed into negatively charged electrons and positively charged nuclei. For fusion to occur the nuclei involved in the reaction need to be close enough, meaning that the Coulomb repulsion between them must be overcome. While in the Sun this is facilitated through the high gravitational pressure, overcoming the Coulomb repulsion is where a serious challenge for fusion on Earth arises. Without the help of gravitational pressure, temperatures on the order of 100 million degrees Kelvin are necessary to achieve fusion reactions, which is about an order of magnitude larger than the temperature in the core of the Sun. No material would be able to hold such hot ionised particles without melting, so the proposed solution for confining a fusion plasma is with the help of strong magnetic fields, which the plasma particles closely follow because they are charged.

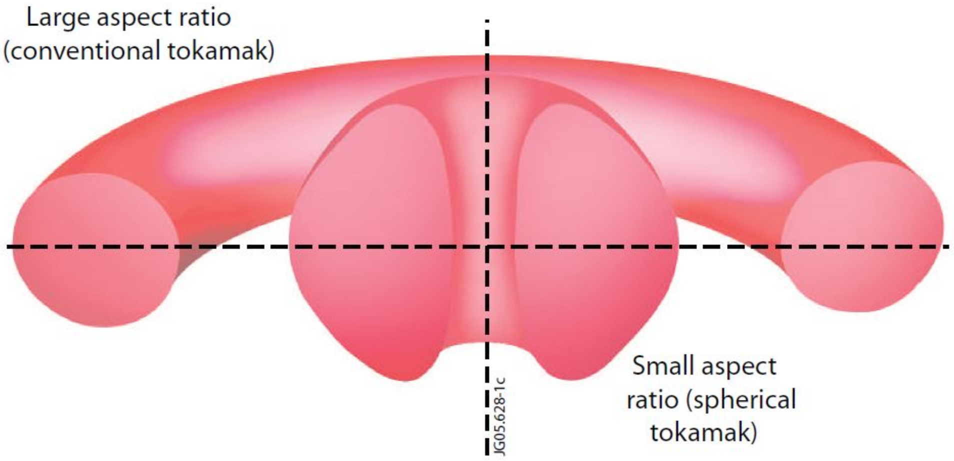

Figure 1.1: Schematic diagram of the relative size and shape of conventional tokamaks compared to spherical tokamaks (image source: Thornton, 2011).

This is called *magnetic confinement fusion* (MCF), and the most promising concept for achieving MCF, to date, is with a toroidal (i.e. doughnut-shaped) reactor called a *tokamak*. Building tokamaks is complicated, time-consuming and costly, with the experimental fusion reactor ITER currently being built in France ranking among the most expensive ground-based science experiments ever, presently estimated at a cost of about 20 billion euros (De Clercq, 2016). The development of any technological system benefits from multiple different units for testing, which means that it is a problem if each unit would cost as much as ITER. For this reason, the more compact, and thus cheaper, *spherical tokamaks* (STs) have long been proposed as component testing facilities to aid the development. STs have a much smaller aspect ratio, i.e. ratio of plasma major radius (R_0) to plasma minor radius (a), than conventional tokamaks, resembling the shape of a cored apple rather than a doughnut, see Figure 1.1.

Beyond the use in component testing, there is an effort to construct STs suitable for energy production in the hope of accelerating the path to commercially available fusion power. Part of this effort is the *Spherical Tokamak for Energy Production* (STEP) program in the UK, aiming to design and construct a prototype fusion energy plant by 2040 (UKAEA, 2022). One phase in the STEP program has been to develop a preliminary high power ST design to understand the interplay between turbulence and shaping for a STEP reactor equilibrium. This design is called BurST, short for *Burning Spherical Tokamak* (Patel, 2021).

Before fusion can enter the market in the form of commercial power plants, there are remaining technological and scientific challenges. One of these is the rare, yet potentially detrimental, occurrence of rapid, unwanted loss of the plasma's magnetic confinement and thermal energy, known as a *disruption*. Even though most of the heat would be isotropically radiated away, the fraction that is transported to the tokamak walls can be significant. These transported heat loads tend to be very localised, which damages the plasma facing components. Since the temperature in the plasma quickly drops during a disruption, the plasma resistivity increases, causing the current flowing in the plasma to decrease. When this happens, currents are induced in the reactor wall leading to structural forces that can be large enough to damage the device. Furthermore, an electric field is induced in the plasma when the plasma current drops, which, if strong enough, can accelerate electrons to relativistic speeds. Such electrons are called *runaway electrons* and they can do severe damage to any area upon which they have an uncontrolled impact, which would lead to tokamaks being out of order for long periods of time during costly repairs.

Even with disruption avoidance systems in place, it will not be possible to prevent every disruption. When they do happen, it is crucial to have systems in place to mitigate their effects through minimising the localised heat loads, getting the plasma current to decrease on a time scale that avoids the strongest structural forces in the wall, as well as through minimising the current carried by runaway electrons that hit the wall. One mitigation approach that can achieve all of this is the injection of material, often a mixture of deuterium and a noble gas.

Runaway electron generation has been studied quite extensively for conventional tokamaks. To date, runaways have rarely been seen in STs during the short disruption timescales in the current small devices, but disruption dynamics are usually different from those in a conventional tokamak (Gerhardt, Menard & the NSTX team, 2009; Thornton, 2011). Furthermore, ST plasmas are typically strongly elongated, and it has been shown that elongated plasmas in a conventional tokamak produce fewer runaway electrons during disruptions (Fülöp *et al.*, 2020). It is therefore not straightforward to transfer the results about runaway electron dynamics in conventional tokamaks to STs, which is the reason for this thesis aspiring to make advances in that direction. The aim is to investigate runaway dynamics in reactor-scale spherical tokamaks, using input parameters for the BurST design as a basis. More specifically, the following questions will be investigated.

- In unmitigated disruptions, what are the respective contributions from different runaway generation mechanisms to the total runaway current?
- Does the energy confinement optimisation of the BurST profiles impact the runaway generation?
- How do changes in relevant physical and structural parameters (e.g. temperature decay rate, wall time accounting for finite resistivity of the structures surrounding the plasma, distance between the plasma and the wall) affect the runaway generation?
- What is the effect on runaway generation due to the evolution of the plasma shape throughout the disruption?
- In what way does including the effect of the compact ST shape through so-called trapping corrections (e.g. including the effect of toroidicity on runaway growth rates) affect the runaway generation?
- How do disruption mitigation strategies based on injecting a mixture of deuterium and neon affect the runaway dynamics?

1.1 Thesis Outline

The results found when investigating the above questions are presented in Section 4.1 for unmitigated disruptions and in Section 4.2 for mitigated disruptions. In order to understand these results, Chapter 2 contains the necessary theory, including how to model a plasma in Section 2.1, specifics of spherical tokamaks in Section 2.2, details about tokamak disruptions in Section 2.3 as well as the cause, generation mechanisms and mitigation strategies of runaway electrons in Section 2.4. Chapter 3 contains a description of the simulation tool, DREAM, and the BurST input data used to obtain the results. Finally, Chapter 5 contains a discussion about the conclusions that can be drawn from the results, as well as some comments about interesting aspects to address in future studies.

2

Theory

In this chapter we give an overview of the theoretical concepts needed to understand the subsequent chapters of this thesis. First, we look into how a plasma can be theoretically described, which later facilitates the understanding of the numerical model presented in Section 3.1. We then move on to theory of spherical tokamaks, after which the details of tokamak disruptions are described. Finally, the *why* and *how* of runaway generation are presented, as well as disruption mitigation approaches.

2.1 Modelling a Plasma

Before we turn to how to model a plasma, it is useful to state its formal definition. Often, the plasma is defined in a qualitative way as *a hot ionised gas of charged particles exhibiting collective behaviour* (Freidberg, 2007; Chen, 2016). This qualitative definition is then accompanied by criteria of more quantitative nature that can be applied in order to determine whether a substance fulfils the plasma definition or not. As a plasma merely consists of atoms decomposed into ions and electrons, it exhibits charge neutrality on a macroscopic scale because a separation of the charges would introduce an excessive electric field acting to remove the separation. This property is called quasi-neutrality. If a single charge would be added to a plasma, particles with opposite charge would surround it, shielding out the electrostatic potential. This phenomenon is called Debye shielding and its effect is that particles located at a significantly larger distance from the charge than a Debye length, given by

$$\lambda_{\mathrm{D}} = \sqrt{\frac{\epsilon_0 T_{\mathrm{e}}}{n_{\mathrm{e}} e^2}}, \tag{2.1}$$

do not experience the particle's electrostatic potential. In Equation (2.1), ϵ_0 is the vacuum permittivity, T_{e} the electron temperature, n_{e} the electron density and e the elementary charge. Debye shielding occurs not only for an introduced charge, but for all ions and electrons in the plasma, leading to a quantitative criterion: the typical length scale, L, of the plasma must be much larger than the Debye length, $L \gg \lambda_{\mathrm{D}}$.

The most accurate way to model a plasma would be to solve equations of motion for each and every plasma particle. However, this is unfeasible due to the large number of plasma particles in any physically interesting plasma system, and we are usually not interested in the position and properties of each individual particle anyway. We are rather interested in macroscopic properties such as density, temperature, current and pressure. To study such aspects, a statistical description of a plasma is useful. In order for a statistical description of a plasma to be valid, another quantitative criterion must be fulfilled, namely that the number of particles in a Debye sphere with volume $4\pi\lambda_{\mathrm{D}}^3/3$ must be large ($\gg 1$).

The first type of plasma model that we introduce here is a so-called *kinetic model*, where apart from the time t, the position $\mathbf{r}$ and momentum $\mathbf{p}$ (or equivalently velocity $\mathbf{v}$) are included in the distribution function, $f(t, \mathbf{r}, \mathbf{v})$, describing each particle species. The distribution function is usually normalised such that the velocity space integral yields the particle density and its evolution is determined by the Boltzmann equation

$$\frac{\partial f}{\partial t} + \mathbf{v} \cdot \nabla f + \frac{Q}{m}(\mathbf{E} + \mathbf{v} \times \mathbf{B}) \cdot \nabla_{\mathbf{v}} f = C(f), \tag{2.2}$$

where Q is the charge, m the mass, $\mathbf{E}$ is the electric field, and $\mathbf{B}$ the magnetic field. The right-hand side of the equation, $C(f)$, is the collision operator, accounting for microscopic interactions between pairs of particles, i.e. interactions on the Debye length scale.

The second type of plasma model, a *fluid model*, is the most relevant one for this thesis because it is used to obtain the presented results. The choice of fluid model for our purposes is discussed further in Section 3.1. In a fluid model the complexity is reduced compared to a kinetic model, as the velocity space is not resolved. The velocity space dynamics are instead accounted for through statistical moments of $f(t, \mathbf{r}, \mathbf{v})$, leading to macroscopic properties based on averages over velocity space volume elements of the plasma. The zeroth, first and second order moments give the density n, macroscopic flow velocity $\mathbf{u}$, and energy density W by

$$n(t, \mathbf{r}) = \int f \mathrm{d}\mathbf{v}, \tag{2.3}$$

$$\mathbf{u}(t, \mathbf{r}) = \frac{1}{n} \int \mathbf{v} f \mathrm{d}\mathbf{v}, \tag{2.4}$$

$$W(t, \mathbf{r}) = \frac{1}{n} \int \frac{1}{2} m |\mathbf{v}|^2 f \mathrm{d}\mathbf{v}. \tag{2.5}$$

One can continue taking higher order moments to obtain other fluid quantities, and the evolution equation for each quantity is obtained by taking the corresponding velocity moment of Equation (2.2).

2.2 Spherical Tokamaks

A tokamak is the most promising concept for achieving a burning plasma to date, as mentioned in Chapter 1, and a schematic illustration is shown in Figure 2.1. In a tokamak, the magnetic field has a toroidal symmetry with twisted field lines, having both a toroidal component, B_φ, and a poloidal component, B_θ (Wesson & Campbell, 2004). There exist closed toroidal surfaces to which the magnetic field and the current are tangential, so-called flux surfaces, which are also illustrated in Figure 2.1. The minor radius coordinate r is defined to be constant on a flux surface and equal to half the width of the flux surface in the mid-plane. Here, the mid-plane is where $Z = 0$, shown as a green circle in Figure 2.1. As r can be used to distinguish the flux surfaces from each other, it is also called flux surface label. The central degenerate flux surface, where $r = 0$ and $R = R_0$, is called the magnetic axis.

The toroidal component of the magnetic field is generated through external magnets and the poloidal component is created by driving a plasma current, I_{tot}, toroidally through the plasma. The reason for twisting the magnetic field lines is that the particles would not be confined with only the externally generated B_φ. This is because the toroidal magnetic field strength is not radially constant, but rather stronger close to the axis of symmetry. The magnetic field strength gradient would lead to vertical particle drifts in opposite directions for oppositely charged particles, with the charge separation causing a vertical electric field. The perpendicular electric and magnetic fields would in turn lead to $\mathbf{E} \times \mathbf{B}-$type forces, making all charged particles drift rapidly in the radial direction and escape from confinement.

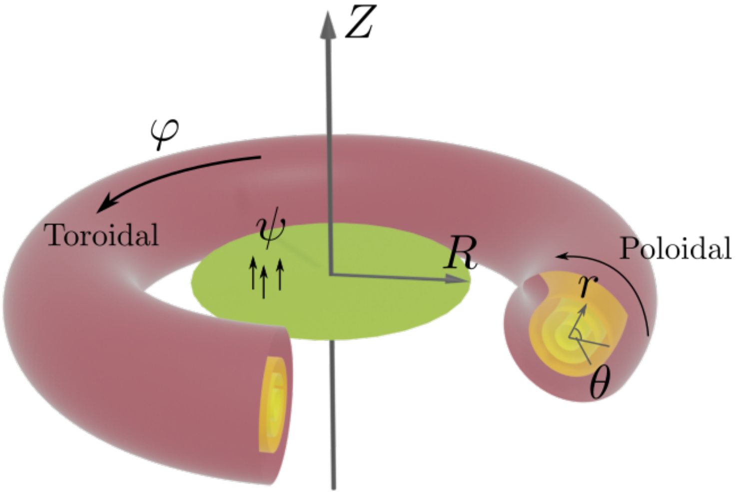

Figure 2.1: Schematic diagram of tokamak geometry. The circular surface perpendicular to the $Z-$axis illustrates the integration surface used to obtain the poloidal magnetic flux ψ at distance R from the axis. In the image, nested flux surfaces are also included (shown in yellow in the cross-section), on which ψ is constant. The location in this toroidal geometry is parameterised by the poloidal angle θ, the toroidal angle φ and the minor radius r (image source: Hoppe, 2021).

To describe how efficient the magnetic field is at confining the plasma, the plasma pressure p normalised by the magnetic pressure (where μ_0 is the vacuum permeability) can be used (Thornton, 2011)

$$\beta = \frac{p}{|\mathbf{B}|^2/2\mu_0}. \tag{2.6}$$

There is an upper limit to the achievable degree of confinement in practice, called the β-limit, which is set by plasma instabilities. The value of the β-limit is sensitive to the size of the tokamak and to the safety factor q, which can be expressed as $\beta_{\mathrm{lim}} \propto \epsilon/q$. Here $\epsilon = r/R$ is the inverse aspect ratio, and q is the average value of the ratio of toroidal revolutions to poloidal revolutions of magnetic field lines on a flux surface. In a circular cross section plasma, this is approximately given by $q = rB_\varphi/RB_\theta$. It is preferable to have a high q from a stability point of view, i.e. many toroidal revolutions to one poloidal revolution, so in order to have a high β-limit allowing for a more efficient magnetic confinement, the inverse aspect ratio at the edge, $\epsilon_a = \epsilon(r = a)$, should be as close to 1 as possible. In conventional tokamaks, ϵ_a is around 0.3, while for spherical tokamaks it is around 0.8. This is one of the main advantages of STs; their compact shape allows for a more efficient confinement for a given magnetic field strength than in conventional tokamaks.

Other advantages of STs to be mentioned are that they require less structural material due to the smaller size, which might lower the construction cost, as well as their naturally occurring high fraction of bootstrap current, which reduces the requirement on the external current drive system (Wilson *et al.*, 2004). The bootstrap current is caused by the presence of magnetically trapped particles that collide with freely passing particles, and at tight aspect ratio (ϵ not being too small) the fraction of trapped particles is higher. Apart from these advantages, there are also some challenges specific to STs, for example needing start-up techniques that do not rely on using the transformer action of a central solenoid to drive the plasma current, as there is very little space to shield it against neutron damage, as well as a smaller available area for heat flux deposition (Lloyd, 2009; Thornton, 2011).

2.3 Tokamak Disruptions

We recall from Chapter 1 that disruptions in tokamaks are off-normal, unwanted events where the plasma magnetic confinement and thermal energy is rapidly lost (Breizman *et al.*, 2019). There are many different causes for disruptions, for example exceeding the β-limit that was mentioned in the previous section. When disruptions occur, the first thing to happen is generally a dramatic decrease of the plasma temperature from the initial 10 keV to 10 eV, within a few milliseconds. This phase is called the *thermal quench* (TQ), and the reason behind it is often heat transport due to flux surfaces breaking up because of plasma instabilities, and radiation by any impurities that have, intentionally or unintentionally, entered the plasma. When the plasma cools, its resistivity increases, preventing the plasma current from flowing as easily. This means that the current begins to decay, characterising the beginning of the second phase of a disruption — the *current quench* (CQ). When the current decays, an electric field is induced in the plasma, as expected from Faraday's law. The faster the current decay, the stronger the induced electric field. If it is sufficiently strong (to be quantified in Section 2.4.1) it can accelerate a significant amount of electrons to relativistic speeds, i.e. generate runaway electrons, which are insensitive to the high bulk plasma resistivity.

The time t_{CQ} it takes for the ohmic component of the current to decay, defined here as (Gerhardt, Menard & the NSTX team, 2009)

$$t_{\mathrm{CQ}} = \frac{t(I_{\mathrm{ohm}} = 0.2 I_{\mathrm{tot},0}) - t(I_{\mathrm{ohm}} = 0.8 I_{\mathrm{tot},0})}{0.6}, \tag{2.7}$$

is important because there are limits on the acceptable CQ times during a disruption. There is both a lower and an upper limit. The lower limit exists because current quenches that are too fast can lead to damage due to substantial torques on the first wall, as wall currents are induced by the rapidly changing plasma current, which causes $\mathbf{j} \times \mathbf{B}-$type forces ($\mathbf{j}$ denotes the current density). The reason for the upper limit is that current quenches that are too slow give the plasma time to move vertically and strike the wall, leading to damaging halo currents (Hollmann *et al.*, 2015). If the number of runaway electrons is large, it aborts the CQ abruptly, meaning that Equation (2.7) is a lower estimate of the CQ time in the absence of runaways. When a significant amount of runaways are generated it stops the total current from decreasing further, achieving a current plateau in which the vast majority of the current is carried by runaways. This is the final phase of a disruption that we consider, called the *runaway plateau*.

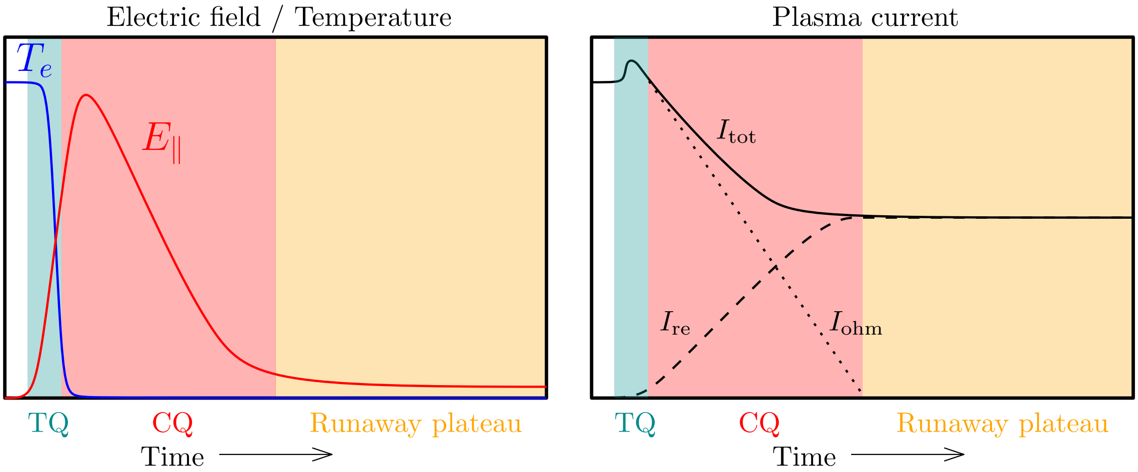

Figure 2.2: Illustration of the evolution of the electric field component parallel to the magnetic field lines, the electron temperature and the plasma current during the three phases of a disruption. In the current evolution image contributions from the ohmic current I_{ohm} and the runaway current I_{re} are also shown separately (image reproduced from: Hoppe, 2021).

The three general phases of a disruption are illustrated in Figure 2.2, where the rapid temperature drop during the TQ, the subsequent current drop during the CQ and the current being carried by the runaway electrons in the runaway plateau are shown.

2.4 Runaway Electrons

As mentioned in the previous section, one of the things that can occur during disruptions is the generation of runaway electrons. Here, we take a closer look at the criteria that need to be fulfilled in order for this to happen.

2.4.1 Criteria for Electrons to Run Away

In a tokamak plasma, electrons can be accelerated by the macroscopic electric field and slowed down by Coulomb collisions with other plasma particles (Freidberg, 2007). The equation of motion parallel to the magnetic field lines for a non-relativistic electron is thus given by

$$\frac{\mathrm{d}v_{\|}}{\mathrm{d}t} = \frac{e}{m_{\mathrm{e}}}|E_{\|}| - \nu v_{\|}, \tag{2.8}$$

where $v_{\|}$ is the velocity component parallel to the magnetic field lines, $E_{\|}$ is the component of the electric field parallel to the magnetic field lines, m_{e} is the electron mass, and ν is the total collision frequency between the electron and other charged particles with density n, given by

$$\nu = \frac{3e^4 n \ln\Lambda}{4\pi\epsilon_0^2 m_{\mathrm{e}}^2 v_{\|}^3}, \tag{2.9}$$

where $\ln\Lambda$ is the Coulomb logarithm that includes the ratio of the lower and upper cut-offs on the energy exchange between colliding particles. Equation (2.9) can be rewritten by normalising with the thermal electron speed $v_{\mathrm{th,e}} = \sqrt{2T_{\mathrm{e}}/m_{\mathrm{e}}}$, yielding

$$\frac{\mathrm{d}}{\mathrm{d}t}\frac{v_{\|}}{v_{\mathrm{th,e}}} = \frac{e}{\sqrt{2T_{\mathrm{e}}m_{\mathrm{e}}}}|E_{\|}| - \frac{3e^4 n \ln\Lambda}{8\sqrt{2}\pi\epsilon_0^2 m_{\mathrm{e}}^{1/2} T_{\mathrm{e}}^{3/2}}\frac{v_{\mathrm{th,e}}^2}{v_{\|}^2}. \tag{2.10}$$

Now, we can replace $v_{\|}/v_{\mathrm{th,e}}$ by $\hat{v}$ and introduce $\hat{E}_{\|}$ and $\hat{\nu}$ for the other parts of the expression, obtaining

$$\frac{\mathrm{d}\hat{v}}{\mathrm{d}t} = \hat{E}_{\|} - \frac{\hat{\nu}}{\hat{v}^2}. \tag{2.11}$$

This is an ordinary differential equation, with a critical point in $\hat{v} = v_{\mathrm{c}} = \sqrt{\hat{\nu}/\hat{E}_{\|}}$. Mathematically, this means that the right-hand side will always be negative if the initial parallel speed is less than the critical speed v_{c}. Analogously, if the initial parallel speed is larger than v_{c}, the right-hand side will always be positive. Physically it means that a too slow electron will decelerate[1] whereas an electron that is fast enough (i.e. with velocity above the critical velocity) will accelerate, continuing until it becomes a relativistic runaway.

The electric field strength necessary for a sizeable fraction of electrons to run away scales with the so-called Dreicer field, $E_{\mathrm{D}} = e^3 n \ln\Lambda/4\pi\epsilon_0^2 T_{\mathrm{e}}$ (Dreicer, 1959). When $E_{\|} = 0.21E_{\mathrm{D}}$ all electrons run away, as this is the electric field strength necessary for an electron with thermal velocity to overcome the frictional drag. In practice, such strong electric fields are never reached during a disruption, but $E_{\|}$ may rather reach a few percent of E_{D}, which is already sufficient to generate a significant runaway population.

The above treatment does not include relativistic effects, which are important when also considering the possibility of runaways being created from already fast electrons. In the relativistic treatment the frictional drag does not tend to zero as $v \to c$, but rather attains a minimum at the critical electric field (Connor & Hastie, 1975)

$$E_{\mathrm{c}} = \frac{e^3 n \ln\Lambda}{4\pi\epsilon_0^2 m_{\mathrm{e}} c^2}. \tag{2.12}$$

---

[1] Note that the approximate expressions in Equations (2.8) and (2.9) are valid at superthermal speeds, but break down at and below thermal speeds. This means that collisions drive the distribution of speeds towards a Maxwellian, rather than slowing it down to zero velocity.

In reality, the value of E_c is even higher, as effects of partially ionised impurities (so-called *partial screening*) and radiation can raise it by up to an order of magnitude (Hesslow *et al.*, 2018*b*; Svensson *et al.*, 2021).

All in all, no runaway electrons are accelerated for electric fields below E_c. For an electric field between E_c and $0.21E_\mathrm{D}$, only a fraction of the available electrons run away. For higher electric fields, of $0.21E_\mathrm{D}$ and above, all electrons run away.

2.4.2 Runaway Electron Generation Mechanisms

There are a number of different mechanisms through which runaway electrons can be generated (Martín-Solís, Loarte & Lehnen, 2017). Most of these belong to the *primary generation* category, not requiring a previously existing runaway seed to produce runaways. Among the primary generation mechanisms we find Dreicer generation, Tritium decay, Compton scattering and hot-tail generation. Dreicer runaway generation is a phenomenon where electrons diffusively leak into the runaway region due to small-angle collisions (Dreicer, 1959). Tritium undergoes β-decay with a half-life $\tau_\mathrm{T} \approx 4500$ days, generating energetic electrons according to a continuous energy spectrum, a part of which may be in the runaway region (Martín-Solís, Loarte & Lehnen, 2017; Fülöp *et al.*, 2020). Due to the wall being activated by the neutrons generated in the fusion process, γ-rays are emitted, which can Compton scatter on the plasma electrons and thereby create energetic electrons that may be in the runaway region. The hot-tail generation mechanism produces runaways due to the fastest electrons not having time to thermalise before the electric field rises, after a sufficiently fast temperature drop during the TQ (Helander *et al.*, 2004; Smith *et al.*, 2005).

There is another category, called *secondary generation*, where close collisions between a runaway electron and a thermal one transfers sufficient energy to the latter so that it also becomes a runaway electron. This leads to an exponential increase in the number of runaway electrons, which is the reason for naming this mechanism avalanche multiplication (Rosenbluth & Putvinski, 1997; Embréus, Stahl & Fülöp, 2018).

Taking all of the above mechanisms into account we can formulate an equation for the time evolution of the runaway electron density n_re,

$$\frac{\partial n_\mathrm{re}}{\partial t} = \gamma_\mathrm{Dreicer} + \gamma_\mathrm{hot\text{-}tail} + \gamma_\mathrm{tritium} + \gamma_\mathrm{Compton} + \Gamma_\mathrm{ava} n_\mathrm{re}. \tag{2.13}$$

Here, each term marks the generation rate of the mechanism indicated by its index. The runaway rates are discussed in more detail in Section 3.1. One could also take into account contributions from advective-diffusive radial transport (Svensson *et al.*, 2021), but that is omitted here as we do not include runaway electron transport in our numerical modelling, as described later.

2.4.3 Runaway Electron Mitigation

When a disruption happens, its impact will have to be mitigated so that the tokamak does not suffer substantial damage. The runaway current should be below 150 kA in order to avoid unacceptable localised melting of the wall, and possibly also underlying structures, if the runaways break free from confinement (Lehnen & the ITER DMS task force, 2021). The current quench time should also be between its defined lower and upper limits, as discussed in Section 2.3. The lower boundary is 20 ms and the time should be shorter than 100 ms (Hender, 2021), or 150 ms as a more relaxed limit imposed by Hollmann *et al.* (2015). Furthermore, the fraction of the thermal energy lost through radial transport should be below 10 %, to avoid unacceptable localised heat loads on the wall (Hollmann *et al.*, 2015).

One of the ways proposed to mitigate these potentially harmful effects and stay within the machine limits is through massive material injection (Hollmann *et al.*, 2015). First, material injection can act to lower the runaway generation, due to the critical runaway energy increasing with the increased electron density. Suitable material for this purpose is deuterium. Massive material injection can also be used to control the current quench time, as t_{CQ} is proportional to the conductivity which depends on the final temperature after the TQ, and this temperature is in turn determined by an equilibrium between the ohmic heating and impurity radiation. Suitable material to inject for this purpose is thus a radiating impurity species. Finally, the injected material can radiate away a large fraction of the thermal energy during the disruption. Suitable for this are the noble gases neon and argon. To accommodate all requirements at once, injection of deuterium and a noble gas is preferred. This has the added benefit that the radiation efficiency is enhanced through the increase in electron density offered by the injected deuterium, as the collisional excitation rate depends on the electron density.

There are different schemes for injecting material into the plasma during a disruption, of which the most studied is gas injection. With this scheme, neutral gas is released into the plasma from a vault in the tokamak wall. Despite this method being favoured due to its simplicity, there is a drawback: the material begins to ionise at the edge of the plasma as soon as it is injected, thus becoming magnetically confined before reaching and cooling the hottest central parts of the plasma. In this thesis, the details of the material delivery are not considered and we work from assumed deposited material profiles. This also facilitates comparison of the results to material injection disruption mitigation effects studied previously in conventionally shaped tokamaks.

3

Simulation Details

Having introduced the necessary theory in the previous chapter, we now turn our attention to the setup of the simulations used to study the runaway dynamics during disruptions in reactor-scale STs. Section 3.1 contains a description of the numerical tool and the model assumptions, while the BurST profiles used as input, as well as additional parameter values, are introduced in Section 3.2.

3.1 DREAM - a Numerical Framework for Disruption Simulations

The numerical framework used to obtain the results in this thesis is called DREAM (*Disruption Runaway Electron Analysis Model*)[1], which is able to self-consistently evolve background plasma parameters together with the runaway dynamics during a disruption. DREAM employs a conventional Newton's method to solve the non-linear system of equations describing the plasma, and a finite volume method to discretise the advection-diffusion type differential equations. The numerical tool is described in detail in (Hoppe, Embreus & Fülöp, 2021), but here we give a brief overview of the model assumptions important for understanding the results in Chapter 4.

For our purposes, DREAM is used in fluid mode, in which the thermal electron bulk, the runaway electrons and the ion species are each treated as a fluid, the principle of which was described in Section 2.1. The various physics mechanisms in fluid mode, such as the runaway generation rates, show good correspondence to the more sophisticated kinetic results, with the model included for processes such as Dreicer generation constructed from large kinetic simulation databases. We do not require inherently kinetic outputs, such as the phase space distribution function, in this scoping study of ST-based reactor scale disruptions and can thus take advantage of the much less computationally demanding fluid mode to perform wide parameter explorations. In the fluid model, the thermal electron bulk is characterised by its density n_e, temperature T_e, and the ohmic current density parallel to the magnetic field lines, j_ohm. In our case, n_e represents the density of all free electrons that are not runaways, i.e. $n_\mathrm{e} = n_\mathrm{free} - n_\mathrm{re}$, and as such it is determined by the evolution of the runaway and free electron densities. The free electron density is defined through the ion composition of the plasma, summed over the charge states, so its evolution depends on the ion densities. The density $n_i^{(j)}$ of ion species i with charge state j is

---

[1] Available at `https://github.com/chalmersplasmatheory/DREAM`

evolved according to the ion rate equation

$$\frac{\partial n_i^{(j)}}{\partial t} = n_\mathrm{e}[\mathcal{I}_i^{(j-1)} n_i^{(j-1)} + \mathcal{R}_i^{(j+1)} n_i^{(j+1)} - (\mathcal{I}_i^{(j)} + \mathcal{R}_i^{(j)}) n_i^{(j)}], \tag{3.1}$$

where $\mathcal{I}$ and $\mathcal{R}$ are ionisation and recombination rates, respectively, which depend on the plasma parameters (Vallhagen *et al.*, 2020). The ions are assumed to be fully ionised at the start of the simulation, as the plasma is assumed to be representative of steady-state operation before the disruption occurs.

The evolution of the runaway electron density n_re is treated according to Equation (2.13). Existing analytical expressions for the Dreicer runaway generation rate γ_Dreicer neglect effects of partial screening, which have been shown to be important (Hesslow *et al.*, 2018*a*). We therefore employ the neural network trained on a large number of kinetic simulations presented in (Hesslow *et al.*, 2019*b*), which take effects of partial screening into account. The model for the tritium decay generation is taken to be as in (Fülöp *et al.*, 2020), with the rate given by

$$\gamma_\mathrm{tritium} = \ln(2) \frac{n_\mathrm{T}}{\tau_\mathrm{T}} F(W_\mathrm{c}). \tag{3.2}$$

Here, n_T is the tritium density, τ_T is the half-life of tritium, mentioned in Section 2.4.2, and $F(W_\mathrm{c})$ is the fraction of electrons generated through tritium decay that have an energy larger than the critical runaway energy W_c. In the model for the hot-tail, an analytic approximate distribution function and critical runaway momentum are calculated as functions of the background plasma parameters and electric field. These are then used to evaluate $\gamma_\text{hot-tail}$, as described in detail in section 4.2 of (Svenningsson, 2020). Compton generation is not included in our current model, due to the lack of input data for the spectrum of γ-photons emitted from the plasma-facing components in a reactor such as BurST. The avalanche multiplication rate is described in (Hesslow *et al.*, 2019*a*), and it accounts for both partial screening and magnetic trapping effects. Magnetic trapping, where an electron is not able to freely move along field lines into regions of high magnetic field strength, is likely substantial at the outer flux surfaces in tight aspect ratio devices if the collisionality is low. This is accounted for by multiplying the avalanche growth rate with a neoclassical factor $\varphi_\epsilon = (1 + 1.46\epsilon^{1/2} + 1.72\epsilon)^{-1/2}$ (Rosenbluth & Putvinski, 1997; Fülöp *et al.*, 2020).

The magnetic geometry is parameterised according to the analytical model described by Miller *et al.* (1998). In this geometry model, the flux surfaces are labelled by r, which measures the half width of a flux surface at the mid-plane (see Section 2.2). The flux surfaces are parameterised by their elongation $\kappa(r)$, Shafranov shift $\Delta(r)$, triangularity $\delta(r)$, reference poloidal flux $\psi_\mathrm{ref}(r)$, and toroidal magnetic field function $G(r) = RB_\varphi(r)$. There is however one difference compared to the original Miller model, namely that the Shafranov shift is shifted such that its value is zero at the magnetic axis (Hoppe, Embreus & Fülöp, 2021). Apart from specifying the above geometrical parameters, the user also inputs the plasma minor radius a, major radius R_0, and wall radius $b = a + r_\mathrm{wall}$, where r_wall is the distance between the plasma and the wall.

The evolution of the electron temperature T_e is prescribed as an exponential decay for the simulations of unmitigated disruptions, whereas the temperature is self-consistently evolved for the mitigated disruptions. The exponential temperature decay is given by

$$T_e(t,r) = T_f(r) + [T_0(r) - T_f(r)]e^{-t/t_0}, \tag{3.3}$$

where $T_0(r)$ is the initial temperature profile, t_0 is the decay time scale and $T_f(r)$ is the final temperature profile. This model has for example also been used by Fülöp *et al.* (2020) and Vallhagen *et al.* (2020). After a disruption, the final temperature T_f is usually flatter than the initial T_0-profile and will therefore be taken as a radially constant value for simplicity. The self-consistent temperature evolution, used in the mitigation simulations, is described by the energy balance equation for the thermal energy density W_e, which relates to the temperature through $W_e = 3n_eT_e/2$. The energy balance equation takes into account ohmic heating by the electric field, electron heat diffusion, bremsstrahlung radiation losses, line radiation losses, and ionisation energy losses (Fülöp *et al.*, 2020; Hoppe, Embreus & Fülöp, 2021; Vallhagen *et al.*, 2022). The energy dependent model for the Coulomb logarithm is described in Equation 18 in (Hoppe, Embreus & Fülöp, 2021), which in the fluid mode is evaluated at a representative runaway momentum of $20\,m_ec$.

The total current density is given by $j = j_{\text{ohm}} + j_{\text{re}}$, where $j_{\text{re}} = ecn_{\text{re}}$ as the runaway electrons are assumed to move with the speed of light c parallel to the magnetic field (Hoppe, Embreus & Fülöp, 2021). The evolution of j is governed by the evolution of the poloidal flux $\psi(r)$ (Hoppe, Embreus & Fülöp, 2021; Pusztai, Hoppe & Vallhagen, 2022). In this evolution, the electric conductivity σ enters, for which we employ a collisional model described by Redl *et al.* (2021), that takes into account the effects of trapping. The boundary conditions for the evolution equation of $\psi(r)$ take into account currents in the passive structures surrounding the plasma, denoted by I_{wall}, via the following set of equations (Pusztai, Hoppe & Vallhagen, 2022)

$$\psi(a) = \psi(b) - MI_{\text{tot}}, \tag{3.4}$$

$$\psi(b) = -L_{\text{ext}}[I_{\text{tot}} + I_{\text{wall}}], \tag{3.5}$$

$$V_{\text{wall}} = R_{\text{wall}}I_{\text{wall}}. \tag{3.6}$$

Here, M is the plasma-wall mutual inductance, L_{ext} is the external inductance, R_{wall} the wall resistance, and V_{wall} the loop voltage in the conducting structure. M is calculated internally in DREAM, whereas L_{ext} and R_{wall} are determined by the user through specifying a resistive timescale of the wall, $t_{\text{wall}} = L_{\text{ext}}/R_{\text{wall}}$. The user thus determines the wall response model by specifying t_{wall}, as well as the aforementioned b (or equivalently r_{wall}).

In the mitigation simulations, the injected material is assumed to be present as a neutral gas at the beginning of the disruption, with a radially constant profile. In the energy balance equation governing temperature evolution, heat transport is included during the material injection simulations, which includes a Rechester-Rosenbluth-type heat diffusion coefficient (Rechester & Rosenbluth, 1978)

$$D_W \approx \pi v_{\text{th,e}} R_0 \left(\frac{\delta B}{B}\right)^2. \tag{3.7}$$

This model requires the user to specify a magnetic perturbation amplitude, $\delta B/B$, that sets the magnitude of the heat diffusivity. Furthermore, the effect of opacity is included in the mitigation simulations by using ionisation and recombination rates for the hydrogen isotopes that are based on the assumption of the plasma being opaque to Lyman radiation. This is included as it has been shown to significantly affect the results by reducing excessive cooling and recombination, and thereby reducing the avalanche growth rate (Vallhagen *et al.*, 2022).

Note that, in light of the above model assumptions, one cannot base quantitative predictions on the results, but they indicate the trends and dependencies of the runaway behaviour in reactor-scale STs.

3.2 Simulation Setup

In this section we discuss specific input parameter values and other simulation setup details used to model disruptions in the BurST reactor scale STs. The BurST input profiles for the initial total current density, electron density and temperature are shown in Figures 3.1a-c (Patel, 2021). The total initial plasma current is $I_{\text{tot},0} = 21\,\text{MA}$. These baseline profiles optimise the energy confinement in BurST. An example of un-optimised profiles, shown as dotted lines in Figures 3.1a-c, are used to study the effect of changes in the input profiles on the results.

In Figure 3.1d the flux surfaces of the input equilibrium are shown. Note that the shaping profiles have been modified in order to avoid multiple magnetic field strength minima on the outer flux surfaces, due to the high-β magnetic well appearing as the poloidal and toroidal magnetic field components become comparable (Wilson *et al.*, 2004), as this is incompatible with the requirements on the input by DREAM. The details of the modifications made to the equilibrium are outlined in Appendix A. The plasma major and minor radii are $R_0 = 3.05\,\text{m}$ and $a = 1.5\,\text{m}$, respectively, and the elongation at the outermost flux surface is $\kappa(a) = 2.8$.

In all simulations, unless stated otherwise, the simulation is ended 150 ms after the beginning of the disruption. This is a representative time scale during which control over the plasma can be maintained after a disruption (Hollmann *et al.*, 2015) and has been used previously for ITER simulations by e.g. Vallhagen *et al.* (2020). An important figure of merit for determining the severity of the runaway problem is the current conversion, defined as the maximum runaway current during the simulation divided by the initial plasma current

$$\text{CC} = \frac{\max(I_{\text{re}})}{I_{\text{tot},0}}. \tag{3.8}$$

The reason for taking the maximum runaway current as opposed to the runaway current at the end of the simulation, which is not necessarily the maximum, is that runaways can be lost to the wall at any time during a disruption. This means that with this definition of CC we obtain the worst case scenario for each simulation.

In the first set of simulations, a scan over the free parameters t_0 and T_f in Equation (3.3) is performed. The parameter ranges scanned over are $t_0 = 0.1\,\text{ms} - 10\,\text{ms}$ and $T_f = 5\,\text{eV} - 40\,\text{eV}$. These ranges are based on experimentally expected values and have also previously been used in similar scans by e.g. Fülöp *et al.* (2020). Note that in an unmitigated disruption t_0 and T_f cannot be chosen; they depend on transport dynamics that cannot self-consistently be calculated within DREAM, as well as on atomic physics, that can be self-consistently calculated.

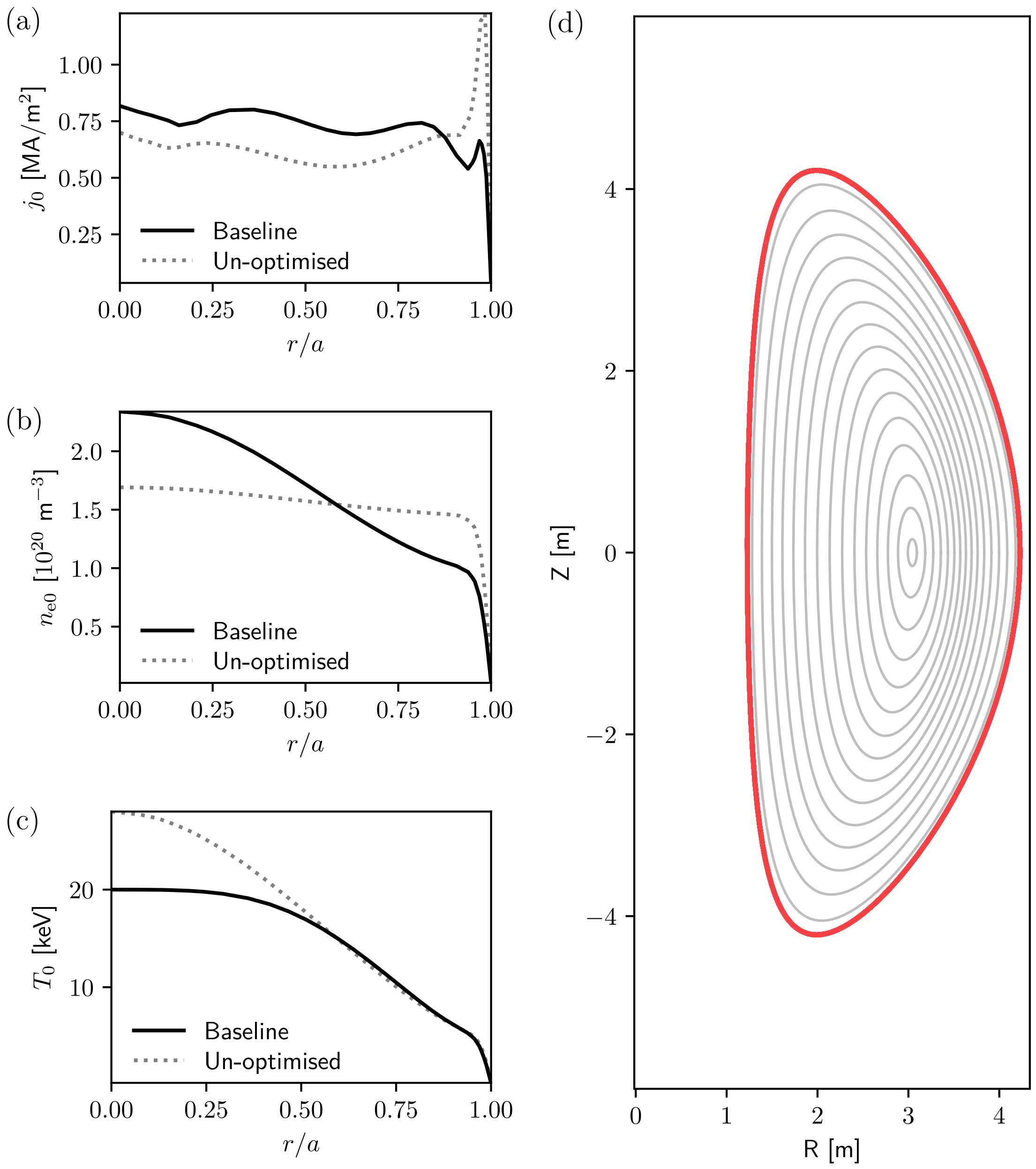

Figure 3.1: Radial profiles for initial (a) current density, (b) electron density and (c) temperature, both for the baseline case (Table 3.1) and the profiles not optimised for energy confinement. (d) Shape of the input equilibrium flux surfaces.

The second set of simulations involves the detailed study of a baseline case with temperature decay parameters near the centre of the scanned ranges, to better understand the runaway dynamics. The numerical values used are summarised in Table 3.1. The sensitivity of the results to certain parameters is also studied. One of the considered variations is the tritium fraction. The composition of deuterium and tritium is chosen to optimise performance, so it is interesting to know how the resulting runaway current is affected by the plasma composition. The effects of changing the wall distance r_{wall} and the wall time t_{wall} are considered as well. The magnetic fields in conducting structures have a complex response to a disruption, which depends on the geometry and material composition. Lacking a detailed model, this response is currently determined by two numbers in DREAM, r_{wall} and t_{wall} (see Section 3.1), and even if a more detailed model would be available for this reactor design it would not be trivial to translate it to these two parameters. They can however be estimated from measurements or detailed electromagnetic calculations, but because of the uncertainty in these values (especially for a preliminary reactor design like BurST), it is useful to let r_{wall} and t_{wall} vary to understand the sensitivity of the result to our assumed values. Furthermore, the plasma shape will in reality evolve during a disruption, so we compare the runaway generation in the highly shaped configuration to a case with no shaping, i.e. a fixed circular cross-section (the j_0 profile shown in Figure 3.1a is then multiplied by 3 to keep the total current constant), to gain an understanding of the impact that shaping can have on the disruption dynamics. The trapping corrections on the generation rates are excluded in one of the variations, as trapping can be expected to be strong in highly shaped compact tokamaks, making it interesting to see exactly how much it impacts the results.

Case	t_0	T_f	Amount T	r_{wall}	t_{wall}
Baseline	1 ms	15 eV	50 %	0 cm	∞

Table 3.1: Summary of parameter values for the baseline case. From left to right the parameters are: TQ decay time scale, TQ final temperature, amount of tritium in the plasma, wall distance, and resistive wall time.

For the material injection simulations the magnetic perturbation $\delta B/B$ is estimated from the values for t_0 and T_f during the TQ, such that the decay time scale before the radiative collapse is approximately t_0. The transport is active during the time it would take for the temperature to decay exponentially (Equation (3.3)) from the initial temperature to 100 eV, after which the MHD-induced losses represented by this perturbation generally no longer dominate. The estimate for the time over which this is active is conservative, as dilution, ionisation and radiation losses generally make the total thermal quench time shorter than this. In reality the flux surfaces tend to reheal after the plasma has lost most of its thermal energy (Sommariva *et al.*, 2018), thus the electron heat diffusivity drops rapidly and a conservative estimate ensures that the transport is active here during the entire TQ. Having significant heat diffusivity after the plasma has reached a low quasi-equilibrium temperature has in fact very little effect, as then radiative heat losses dominate by a large factor.

Trapping corrections to the growth rates are also turned off for the material injection simulations, as these effects are negligible at high densities and in the presence of significant impurity content, due to the high collisionality. Also, trapping is less important in the presence of very high electric fields, as particles can be accelerated out from the trapped region in less than their toroidal orbit time (McDevitt & Tang, 2019). The same assumption was made by Vallhagen *et al.* (2020).

In Section 2.4.3, the reason for mitigation strategies based on injecting a mixture of deuterium and a heavy impurity was discussed, and for our purposes the impurity is chosen to be neon. The reason for choosing neon over argon is that for similar ITER-simulations it is shown that the suitable parameter range is smaller with argon (Vallhagen *et al.*, 2020), due to the increased number of electrons enhancing the avalanche multiplication (Hesslow *et al.*, 2019*a*). We identify trends in the impact of material mitigation by scanning the injected deuterium and neon densities over the ranges $n_{\mathrm{D}} = 10^{20}\,\mathrm{m}^{-3} - 10^{22}\,\mathrm{m}^{-3}$ and $n_{\mathrm{Ne}} = 10^{16}\,\mathrm{m}^{-3} - 10^{20}\,\mathrm{m}^{-3}$, which are similar to the ones previously used by Vallhagen *et al.* (2020).

4

Results

The results found when investigating the questions stated in Chapter 1 are presented and discussed in the chapter that follows. Section 4.1 demonstrates the scale of the problem by showing the level of runaway generation in unmitigated ST reactor disruptions, and the lack of sensitivity to all input parameters investigated. In Section 4.2 the improvements that can be achieved with material injection mitigation strategies are demonstrated.

4.1 Unmitigated Disruptions

In this section we follow the plan outlined in Section 3.2, first turning our attention to the effect of the temperature decay during the TQ on the evolution of the current components in the subsequent CQ, to explore the scale of the runaway problem depending on the free parameters t_0 and T_f of the exponential temperature decay model. Next, the baseline case summarised in Table 3.1 is studied to improve our understanding of the underlying runaway dynamics. Lastly, the sensitivity of the results for the baseline case to a number of parameter and model choices is investigated, summarising the results in Table 4.1.

4.1.1 Temperature Decay Parameter Scan

When studying the evolution of the current components during the CQ, we consider specifically the fraction of the initial current converted to runaways, as well as the decay time scale of the ohmic current. The temperature evolution is modelled by an exponential decay as described by Equation (3.3), where the decay time scale t_0 and final temperature T_f are free parameters, which is the reason we scan over the experimentally expected ranges. We remind the reader that when disruptions happen, t_0 and T_f are not something that one can “choose” in any way because of their dependence on the transport and atomic physics at play. This means that the results in Figure 4.1 indicate the severity of runaway generation in reactor-scale STs depending on the temperature decay parameter values. In Figure 4.1a we see that the runaway production is high when the cooling is rapid ($t_0 < 1\,\mathrm{ms}$), while the dependence on the temperature reached after the TQ is not very strong in this region. For slower cooling rates ($t_0 > 1\,\mathrm{ms}$), however, the current conversion can differ by an order of magnitude depending on the final temperature, with higher values for lower temperatures. The region where the runaway generation is the least problematic for unmitigated disruptions is when $t_0 > 3\,\mathrm{ms}$, where the runaway current would be lower than 21 kA, i.e. well below the 150 kA limit discussed in Section 2.4.3. In the rest of the $t_0 - T_f$ space some form of mitigation would be necessary to keep the maximum runaway current below this limit.

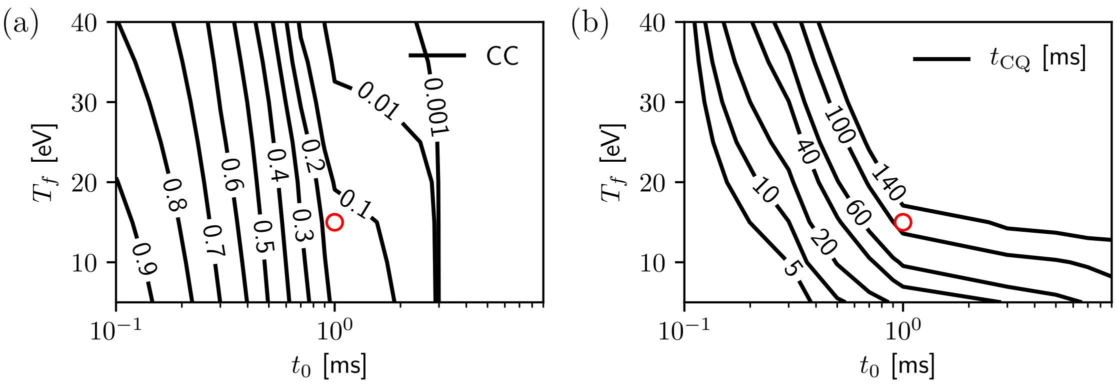

Figure 4.1: Contours of (a) current conversion defined in Equation (3.8) and (b) CQ time t_{CQ} as functions of decay time scale t_0 and final temperature T_f of the exponential temperature decay in Equation (3.3). The red circle marks the case where $t_0 = 1\,\mathrm{ms}$ and $T_f = 15\,\mathrm{eV}$, our baseline case, which is studied in more detail in Section 4.1.2. Apart from t_0 and T_f the parameters are the same as in Table 3.1.

Comparing Figure 4.1b to Figure 4.1a, we see that the current conversion is in general high when t_{CQ} is short. This connection can be understood by noting that the faster the current drops during the CQ, the higher the induced electric field, which in turn increases the severity of runaway acceleration. Furthermore, we see in Figure 4.1b that in the region where the current conversion is the lowest ($t_0 > 3\,\mathrm{ms}$), the CQ time is strongly dependent on the final temperature, such that t_{CQ} is below the 100 ms or 150 ms limit discussed in Section 2.4.3 only if the plasma temperature falls below approximately 15 eV after the disruption. This means that in order to satisfy both demands on the current conversion as well as on the CQ time, mitigation strategies would be necessary not only when $t_0 < 3\,\mathrm{ms}$, but also when $T_f \gtrsim 15\,\mathrm{eV}$ in the region where $t_0 > 3\,\mathrm{ms}$.

4.1.2 Baseline Case

In order to get more insight into the runaway dynamics at play, we take a close look at a case near the centre of the scanned parameter space. This case, with $t_0 = 1\,\mathrm{ms}$ and $T_f = 15\,\mathrm{eV}$, is marked with a red circle in Figure 4.1 and its plasma current, electric field and temperature evolution are shown in Figure 4.2. The time evolution of the radial distributions of runaway rates for the different mechanisms are plotted in Figure 4.3. In Figure 4.2c the temperature decay during the TQ with $t_0 = 1\,\mathrm{ms}$ and $T_f = 15\,\mathrm{eV}$ in Equation (3.3) is shown and in Figure 4.2a we see how the current decays during the CQ. The current conversion, defined in Equation (3.8), at these temperature decay parameters is 13.89 % and t_{CQ} is 114.4 ms, meaning that this disruption would not be tolerable without mitigation in reactor-scale spherical tokamaks due to the large runaway current generated. Figure 4.2b shows that the maximum of the electric field is about 10 V/m, which is not sufficient to make the Dreicer contribution to the runaway generation significant, as is evident from Figure 4.3a. The runaway production is the largest on axis but also has contributions for larger radii, as shown in Figure 4.2d. This is a difference from similar results for tokamaks with a more conventional shape, where the production only has the on-axis peak and exponentially drops to zero for larger radii (Fülöp *et al.*, 2020).

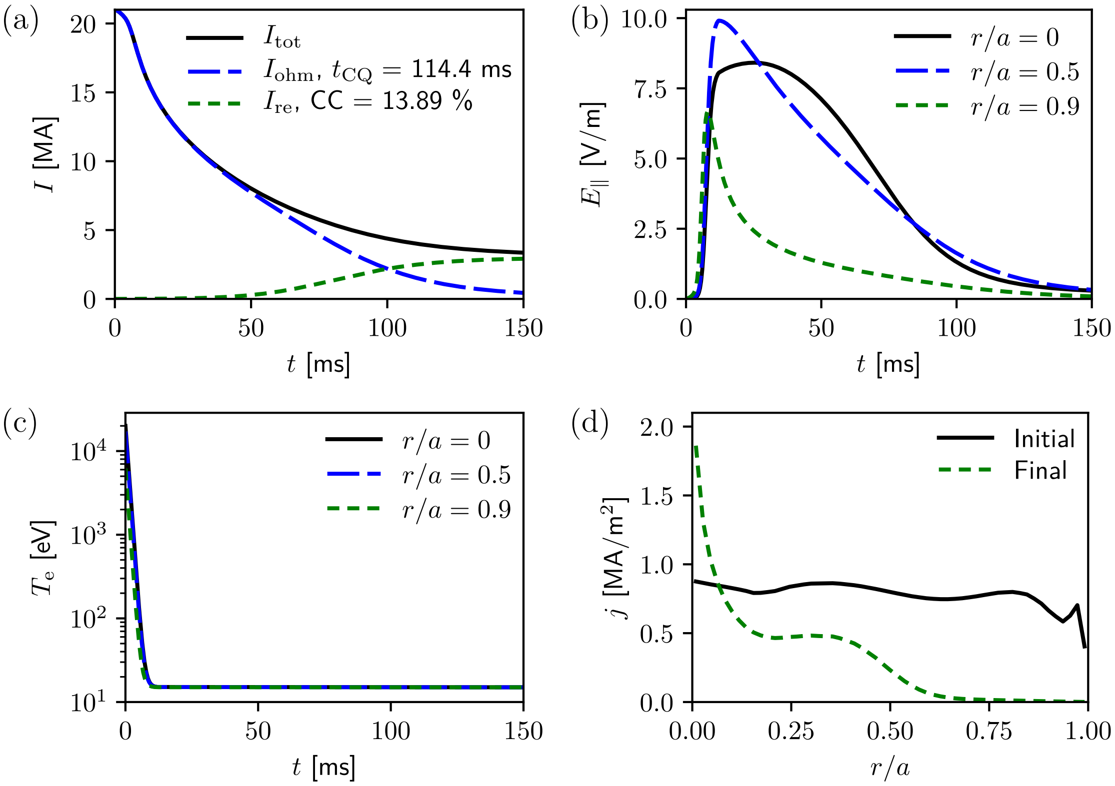

Figure 4.2: Plasma current, electric field and temperature evolution in the baseline case where $t_0 = 1\,\mathrm{ms}$ and $T_f = 15\,\mathrm{eV}$. (a) Total plasma current (solid) as function of time, together with the ohmic (long dashed) and runaway (short dashed) contributions. (b, c) Electric field and electron temperature evolution at different radii, given in the legend. (d) Initial and final radial current density profiles.

In Figure 4.3c we can see that the dominant primary generation mechanism is hot-tail, as its maximum value is about six orders of magnitude larger than that of the second most important mechanism, the tritium decay shown in Figure 4.3b. As the hot-tail generation happens very early during the disruption, where transport may be strong due to a high level of magnetic fluctuations, this result is likely to overestimate the hot-tail seed at the end of the TQ because transport has not been taken into account. When completely disabling the hot-tail seed, but otherwise using identical settings, the runaway conversion plummets to 0.0001 %, see Table 4.1, so 13.89 % can be taken as an upper limit for the current conversion in this case. Note, however, that $t_{\rm CQ}$ is longer in the case where hot-tail generation is excluded and the current quench is incomplete after 150 ms, with about 2.1 MA ohmic current remaining. The residual ohmic current could potentially convert to runaway current beyond this point. However, when running this simulation for twice as long, i.e.

until 300 ms, the resulting current conversion is instead 0.0005 %. This means that the runaway current is about 0.1 kA, still well below the limit, and the remaining ohmic current is about 0.3 MA, so if the entire hot-tail seed would be lost to radial transport this is a disruption where mitigation would not be necessary.

In Table 4.1 we summarise the CC, t_{CQ} and remaining ohmic current for a number of different cases, including the baseline entry at the top. That the influence of tritium decay on the runaway rate is weak is further evident from Table 4.1; neither the current conversion nor the CQ time is affected when altering the amount of tritium in the plasma to the two limiting cases of pure deuterium and pure tritium. The overall dominant runaway mechanism is avalanche multiplication, with a maximum value of about two orders of magnitude larger than the hot-tail maximum, and with high rates for a much longer period of time, as seen in Figure 4.3d. As the avalanche gain increases exponentially with the plasma current, it is no surprise that avalanche is the dominant runaway generation mechanism in this case where there is a high initial plasma current. Due to the dominance of the avalanche, the total runaway generation rate is almost identical to the avalanche rate and is therefore not shown separately. Also, it can be noted that there is a region with negative avalanche multiplication, which occurs when the electric field is below the critical electric field. The reason behind it is the possibility for a runaway electron to lose enough energy when colliding with the thermal electron bulk that it falls out of the

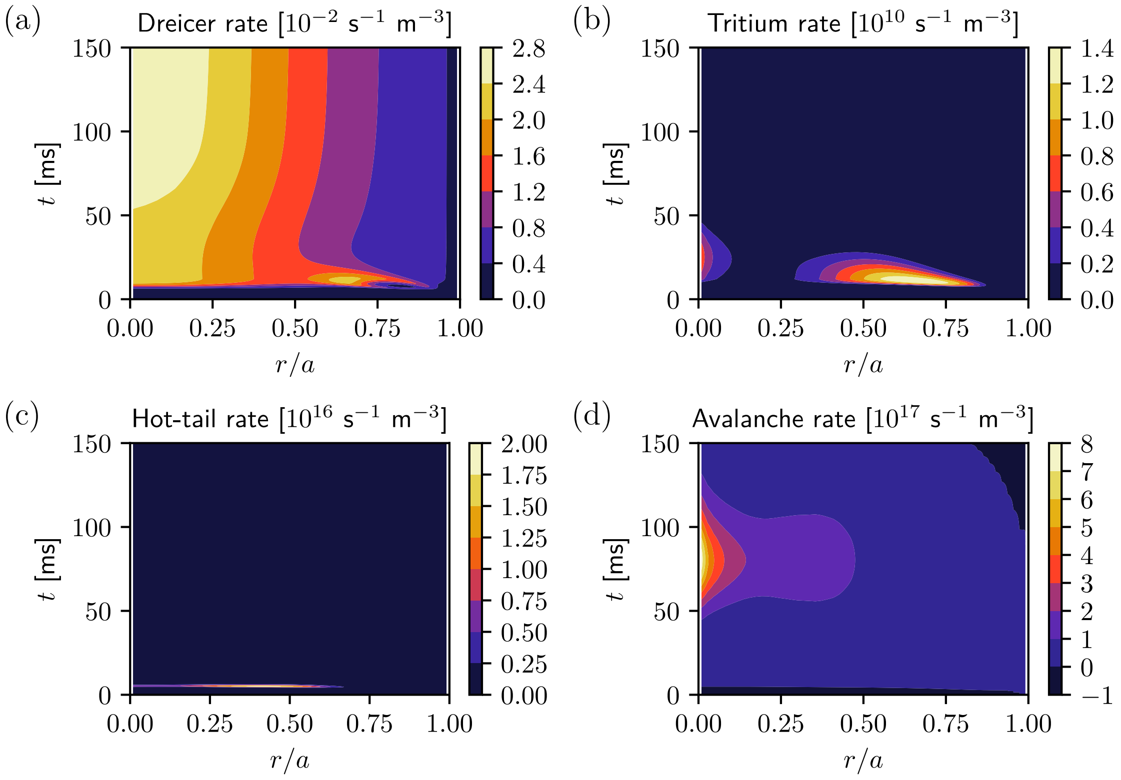

Figure 4.3: Time evolution of the radial distributions of the (a) Dreicer, (b) tritium decay, (c) hot-tail and (d) avalanche runaway rates, in the baseline case where $t_0 = 1$ ms and $T_f = 15$ eV.

runaway region, without knocking the thermal electron into the runaway region. This means that the runaway density decreases in time.

4.1.3 Parameter Sensitivity

To obtain the results presented thus far, a number of model and parameter choices were made, as described in Chapter 3. It is important to gain insight into the impact of these choices, so to this end the current conversion and t_{CQ} were evaluated for a number of variations to the baseline. The results are listed in Table 4.1, together with the remaining ohmic current for each case.

Case	CC	t_{CQ}	Remaining I_{ohm}
Baseline	13.89 %	114.4 ms	0.44 MA
No hot-tail	0.0001 %	145.0 ms	2.1 MA
0 % tritium	13.89 %	114.4 ms	0.44 MA
100 % tritium	13.89 %	114.4 ms	0.44 MA
No shaping	30.42 %	40.6 ms	0.07 MA
No trapping	23.83 %	86.3 ms	0.22 MA
$r_{\mathrm{wall}} = 10\,\mathrm{cm}$	23.60 %	123.5 ms	0.71 MA
$r_{\mathrm{wall}} = 30\,\mathrm{cm}$	37.29 %	124.7 ms	1.4 MA
$t_{\mathrm{wall}} = 500\,\mathrm{ms}$	28.88 %	209.8 ms	3.9 MA
$t_{\mathrm{wall}} = 10\,\mathrm{ms}$	60.36 %	119.4 ms	2.9 MA

Table 4.1: Current conversion, CQ time t_{CQ}, and remaining ohmic current at the end of the simulation (150 ms) for deviations from the baseline case.

First we consider the effect of the compact ST shaping on the results, recalling from Section 3.2 that the reason for studying these variations is that trapping can be expected to be strong in highly shaped compact tokamaks. We note that both the case where trapping effects on the runaway generation mechanisms are excluded (*no trapping*), as well as the case with a circular cross section (*no shaping*), increase the current conversion and decrease the CQ time. The physical reasons behind these changes are however different in the two cases. In Figure 4.4a and Figure 4.4b the electric field and the current density profiles of these two cases are shown, together with the baseline case for comparison. The maximum electric field is notably higher in the *no shaping* case, which is the reason for the increased current conversion. In the *no trapping* case the maximum electric field is the same but the current contributions from larger flux surfaces — where a significant fraction of particles would otherwise be trapped — are increased, as seen in the radial distribution of the final current density.

The effect of the containment structure on the result is embodied in the wall distance and wall time. Altering the wall distance from $r_{\mathrm{wall}} = 0\,\mathrm{cm}$ and the wall time from that of a perfectly conducting wall ($t_{\mathrm{wall}} = \infty$) also both lead to increased CC, as well as increased t_{CQ}. The electric field and the current density for these cases can be seen in Figures 4.4c and 4.4d. In both cases the off-axis contributions are increased compared to the baseline, which in the r_{wall} case is due to magnetic energy returning to the plasma from the vacuum region between the plasma and

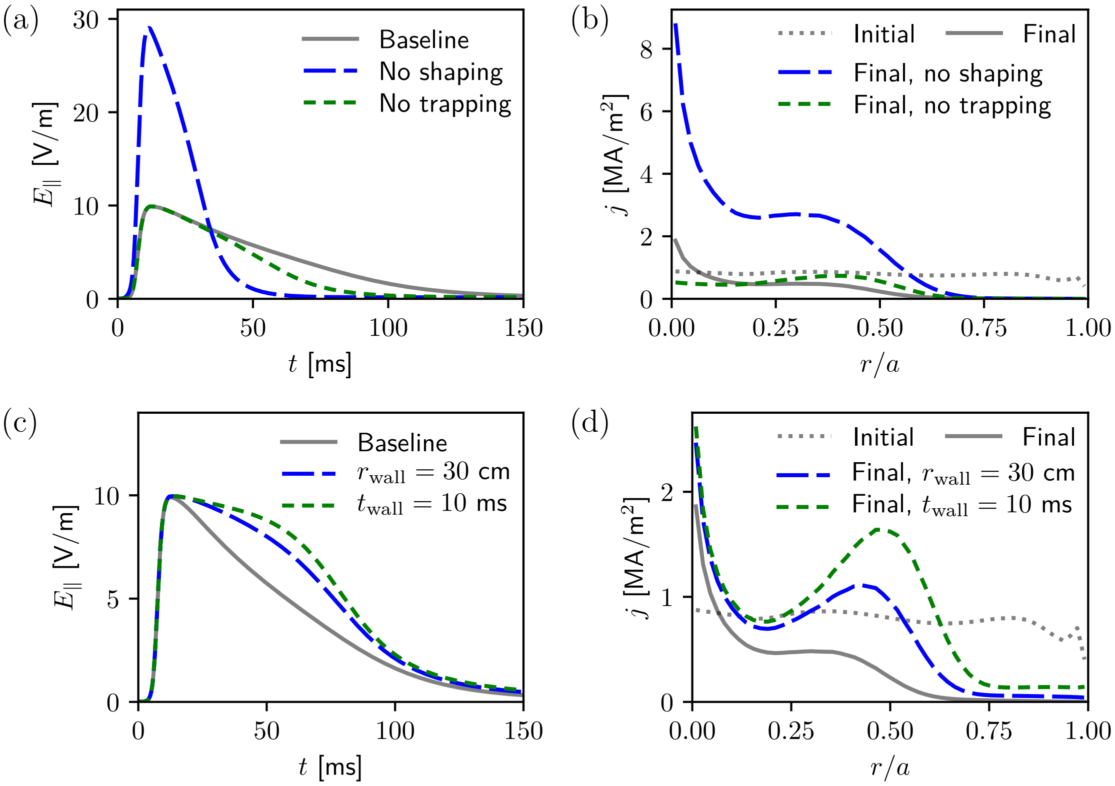

Figure 4.4: Electric field evolution at $r/a = 0.5$ (a, c) and final current densities (b, d). Panels (a, b) compare the baseline (solid) with the *no shaping* (long dashed) and *no trapping* (short dashed) cases. Panels (c, d) compare the baseline ($r_{\rm wall} = 0\,$cm, $t_{\rm wall} = \infty$, solid) with the cases using $r_{\rm wall} = 30\,$cm (long dashed) and $t_{\rm wall} = 10\,$ms (short dashed). In (b, d) the initial current density profile is also included (dotted).

the wall, while in the $t_{\rm wall}$ case it is magnetic energy from the wall and possibly the surrounding structures that diffuses back into the plasma. The stronger electric fields near the edge affect the generation mechanisms, such that more runaway production happens further away from the centre of the plasma. This is visible in the final current densities, which have a larger off-axis contribution. Another interesting observation concerning changing to a finite wall time is that the dynamics of the total current changes as a result of the amount of energy that returns from the wall. The effect of this is that a runaway plateau phase is not immediately reached after the CQ, but there is rather a long gradual increase in the runaway current before the plateau is reached. This is illustrated in Figure 4.5a. Note the long time scale needed to reach the plateau in this case; it is much longer than the 150 ms cut-off where the control over the plasma is deemed lost after a disruption, meaning that the runaway current would depend quite strongly on when the control over the plasma is lost, as compared to the case of a perfectly conducting wall.

The final column of Table 4.1 indicates the remaining ohmic current at the end of the simulations. Values more than tens of kiloamperes indicate an incomplete current quench and we see that this is the situation in all variations evaluated. As noted above, the remaining ohmic current could become a problem, because it might

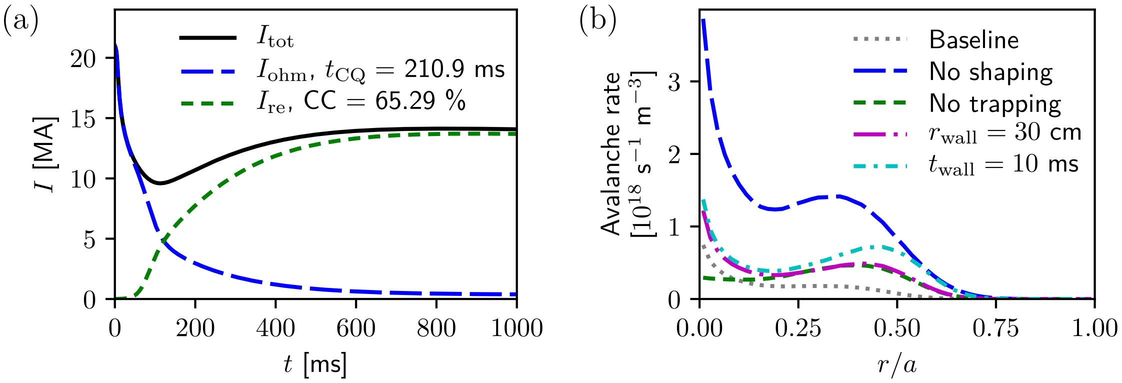

Figure 4.5: (a) Total plasma current (solid) as a function of time, together with the ohmic (long dashed) and runaway (short dashed) contributions, when using a finite wall time $t_{\rm wall} = 500\,\mathrm{ms}$. Note the long time scale and compare to Figure 4.2a. (b) Characteristic radial profiles of the avalanche runaway rate: baseline case (dotted, see Figure 4.3d), *no shaping* case (long dashed), *no trapping* case (short dashed), $r_{\rm wall} = 30\,\mathrm{cm}$ case (long dash-dotted), and $t_{\rm wall} = 10\,\mathrm{ms}$ case (short dash-dotted).

convert to runaway current if control over the plasma is lost beyond this point. The case with the most residual ohmic current is that with a wall time of 500 ms (almost 9 times that in the baseline) and the case with the least is the *no shaping* case (around 6 times lower than that in the baseline). Therefore we see that the strong ST shaping is making the residual ohmic current problem worse, whilst it reduces the initial runaway problem.

Regarding the different generation mechanisms, we have already touched upon the weak influence of the tritium seed, as confirmed by the cases where the amount of tritium is varied. In all other cases tritium generation remains of the same order of magnitude. When and where the tritium runaway generation happens does however change, an example being the radial gap at around $r/a \approx 0.25$ in Figure 4.3b disappearing in the *no shaping* and *no trapping* cases. In all cases in Table 4.1 hot-tail is the dominant primary generation mechanism, whereas avalanche is the dominant mechanism. When varying parameters, the only case which produces a change in the hot-tail generation compared to Figure 4.3c is the *no shaping* case, where the electric field is stronger. In this case the hot-tail generation happens at the same radii during the same time period, but the maximum value is increased by a factor of around five. As the avalanche multiplication dominates in all studied cases, it determines the shape of the final current density, which can be seen by comparing the profile of the avalanche rates for the parameter variations studied, as shown in Figure 4.5b, to the final current profiles in Figures 4.4b and 4.4d.

Finally, when using the input plasma density and temperature not optimised for energy confinement (dotted lines in Figures 3.1a-c) with otherwise the same parameters as in the baseline case, the current conversion is 21.91 %, compared to 13.89 % in the baseline case. This means that the profiles optimised for energy confinement also reduce the runaway production. We studied again the effect of the parameter variations listed in Table 4.1 for these un-optimised energy confinement profiles, and we found the same trends in the runaway current conversion as for the baseline profiles; the runaway current conversion stays the same or increases. This indicates that there is a robustness in the obtained results with respect to changes of this type in the input profiles.

All in all, we have seen here in Section 4.1 that we expect runaway generation in STs as well, and that the level is similar to that found in previous studies for conventional tokamaks, e.g. by Fülöp *et al.* (2020).

4.2 Mitigation with Massive Material Injection

Having studied the severity of unmitigated disruptions in reactor-scale STs in the previous section, we will in this section consider the effectiveness of material injection mitigation on the runaway dynamics. The considered mitigation strategy is injection of a large quantity of mixed deuterium and neon, as described in Section 3.2. Also recall from Section 3.1 that the injected material in the current model is uniformly deposited at the start of the simulation.

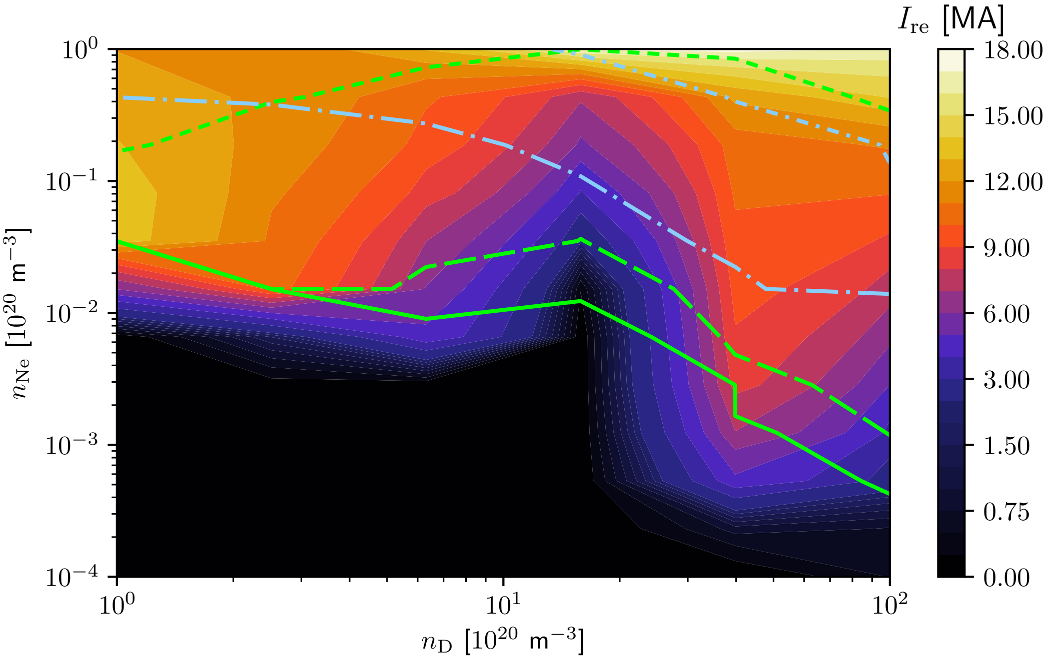

Figure 4.6: Maximum runaway current $I_{\rm re}$ as a function of injected deuterium ($n_{\rm D}$) and neon ($n_{\rm Ne}$) densities, in the case where $\mathrm{d}B\,/B \approx 0.6\,\%$. Between the short- and long-dashed lines, $t_{\rm CQ}$ takes values between 20 ms and 100 ms. Below the solid line, $t_{\rm CQ}$ is longer than 150 ms or not calculable with Equation (2.7) due to the CQ being incomplete (in which case the CQ time would be much longer than 150 ms). Above the dash-dotted lines the transported fraction of the thermal energy loss is lower than 10 % (short dash-dotted) and 80 % (long dash-dotted), respectively.

We consider mitigation of two cases, one representative of a fast TQ ($t_0 = 1\,$ms, $T_f = 10\,$eV) and one of a slow TQ ($t_0 = 10\,$ms, $T_f = 10\,$eV). The magnetic perturbation determining the transport was estimated based on the two sets of temperature decay parameters, as described in Section 3.2. With $t_0 = 1\,\mathrm{ms}$, $T_f = 10\,\mathrm{eV}$ (high transport) the corresponding unmitigated case has a CC of 46.30 %, or equivalently a maximum runaway current of 9.7 MA, and $t_{\mathrm{CQ}} = 75.2\,\mathrm{ms}$, so in this case the mitigation objective is to reduce the runaway current while keeping the CQ time within the limits. With $t_0 = 10\,\mathrm{ms}$, $T_f = 10\,\mathrm{eV}$ (low transport) the corresponding unmitigated case has a CC of 0.0 %, but an incomplete CQ with an ohmic current of 8.7 MA remaining at the end of the simulation. The goal of mitigation in this case is thus instead to make the ohmic current decay faster to obtain a t_{CQ} between the limits, while keeping the runaway current at a low level.

The resulting maximum runaway current as a function of injected deuterium and neon is shown in Figure 4.6 for the case with high transport and in Figure 4.7 for the case with low transport. The figures also include several boundaries: lower t_{CQ} boundary of 20 ms (short dashed), two possible upper t_{CQ} boundaries of 100 ms (long dashed) and 150 ms (solid), as well as boundaries indicating the fraction of the thermal energy that is lost through radial transport (10 % short dash-dotted and 80 % long dash-dotted). As can be seen in Figures 4.6 and 4.7, there is a region of low runaway current (below 0.5 MA) for low densities, as well as at high neon and low deuterium density in the low transport case. The reason for the existence of these regions of low runaway current is mainly that the ohmic CQ is incomplete. This is evident from the regions being below or to the left of the solid lines, indicating that the injected deuterium-neon mixture is insufficient to induce a complete radiative collapse.

In Figure 4.6 we see that in the region between the lower t_{CQ} limit of 20 ms and the upper t_{CQ} limit of 100 ms, runaway currents between 2.5 MA and 18 MA are obtained. If the upper CQ time limit is instead taken to be 150 ms, the region contains runaway currents down to 0 MA, around injected densities of $n_{\mathrm{D}} \approx 1.6 \cdot 10^{21}\,\mathrm{m}^{-3}$ and $n_{\mathrm{Ne}} \approx 1.5 \cdot 10^{18}\,\mathrm{m}^{-3}$. Hence, it is favourable from a runaway current point of view to allow the more relaxed upper t_{CQ} limit.

The landscape of the maximum runaway current is different for lower magnetic perturbations, as seen in Figure 4.7. Nonetheless, the runaway currents obtained within the CQ time limits are comparable. Thus, both in the case of a fast TQ (where mitigation is needed to reduce the runaway current while keeping the CQ time within acceptable limits, Figure 4.6), as well as the case of a slow TQ (where mitigation is needed to reduce the CQ time while keeping the runaway current low, Figure 4.7), an injected mixture with densities of around $n_{\mathrm{D}} \approx 1.6 \cdot 10^{21}\,\mathrm{m}^{-3}$ and $n_{\mathrm{Ne}} \approx 1.5 \cdot 10^{18}\,\mathrm{m}^{-3}$ offers the possibility of achieving tolerable runaway current and ohmic current evolution simultaneously.

We look in more detail at the region in Figure 4.6 where the best performance in terms of low runaway current is being obtained, that is $n_{\mathrm{D}} \approx 1.6 \cdot 10^{21}\,\mathrm{m}^{-3}$ and $n_{\mathrm{Ne}} \approx 1.5 \cdot 10^{18}\,\mathrm{m}^{-3}$, and find that the tritium, hot-tail and avalanche all behave differently than in the corresponding unmitigated case. Hot-tail is still the dominant primary seed, although the maximum generation rate is reduced from $\sim 10^{16}\,\mathrm{s}^{-1}\mathrm{m}^{-3}$ to $\sim 10^{7}\,\mathrm{s}^{-1}\mathrm{m}^{-3}$. Also, the generation only occurs over about 0.5 ms, compared to 2 ms in the unmitigated case, and is localised inside a more limited radial range around the plasma centre (up to $r/a \approx 0.6$ rather than $r/a \approx 1.0$). With this combination of injected deuterium-neon densities the fast electrons that

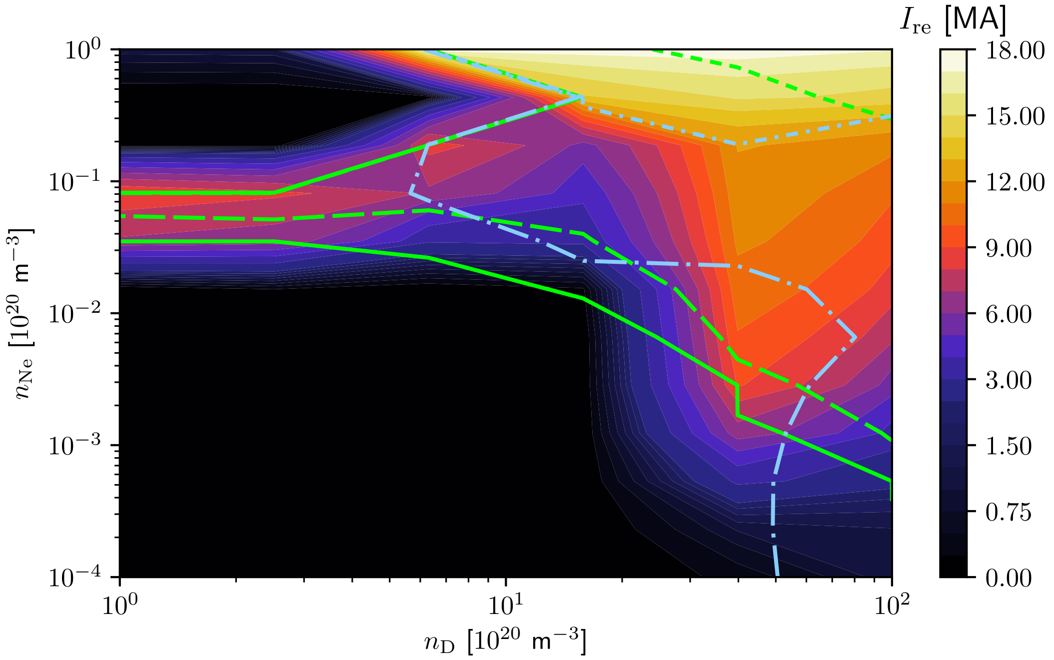

Figure 4.7: Maximum runaway current I_{re} as a function of injected deuterium (n_{D}) and neon (n_{Ne}) densities, in the case where $\mathrm{d}B\,/B \approx 0.2\,\%$. Between the short- and long-dashed lines, t_{CQ} takes values between 20 ms and 100 ms. To the left of the solid lines, t_{CQ} is longer than 150 ms or not calculable with Equation (2.7) due to the CQ being incomplete (in which case the CQ time would be much longer than 150 ms). Above the dash-dotted lines the transported fraction of the thermal energy loss is lower than 10 % (short dash-dotted) and 80 % (long dash-dotted), respectively.

formed the hot-tail in the unmitigated case slow down more before the electric field rises, leading to a smaller "tail" that can be converted to runaways. The tritium seed is here fully suppressed, which indicates that the critical runaway energy for generation through tritium decay (see Equation (3.2)) is increased for this level of impurity injection, in accordance with results by Vallhagen *et al.* (2020). The smaller runaway seed currents lowers the outcome of the avalanche multiplication, leading to the observed low runaway current. A word of caution, however: the largest increase in the avalanche multiplication is here observed at the very end of the simulation. This is in accordance with (Hesslow *et al.*, 2019*a*), where the runaway generation is first suppressed by material injection, to later become large due to a stronger avalanche in the presence of heavy impurities. There is also about 1.4 MA ohmic current left, which thus could readily be converted to a runaway current beyond the 150 ms mark.

If we now also, apart from the t_{CQ} limit, would take the limit on transported thermal energy loss into account, we see that there is no region where it is possible to fulfil all three demands simultaneously in either case. In the region above the short dash-dotted line where the transported fraction is below 10 %, the runaway current is at least 11 MA. Even if it would be possible to tolerate a transported fraction of 80 %, the lowest runaway current reached is 4 MA in the case of high transport, and 2.5 MA in the case of low transport, both above the tolerable limit.

The reason behind the transported fraction reaching this magnitude seems to be the shape of the initial temperature and density profiles, see Figures 3.1b-c. For example, in the case with the lower $\delta B/B$ for $n_{\mathrm{D}} \approx 1.6 \cdot 10^{21}\,\mathrm{m}^{-3}$ and $n_{\mathrm{Ne}} \approx 8.1 \cdot 10^{18}\,\mathrm{m}^{-3}$, the transported fraction is 61 %. If we instead change to a flat initial density of $n_0 = 10^{20}\,\mathrm{m}^{-3}$, as in (Vallhagen *et al.*, 2020), the transported heat loss fraction is reduced to about 33 %. If also the temperature profile is changed to the one of (Vallhagen *et al.*, 2020), i.e. $T_0(r) = 20 \cdot [1 - (r/a)^2]\,\mathrm{keV}$, the fraction is further reduced to 14 %, very close to the acceptable level. Regardless of the temperature and density profiles used for this particular case, we also see a peak in the final current density profiles at the very edge of the plasma. This is different from the final current density profiles that we have seen in previous cases, but it would perhaps not be a robust feature if particle transport would be included in the simulations, as this would act to transport the edge runaways out of the plasma.

All in all, we can conclude from this section that the quantity of neon and deuterium needed for mitigation as modelled here is similar to that for conventional tokamaks. In can also be concluded that fulfilling the runaway current limit and the CQ time limits is possible simultaneously, but not while also fulfilling the limit on the transported thermal energy loss fraction.

5

Concluding Remarks

The aim of this thesis has been to investigate runaway dynamics during disruptions in reactor-scale spherical tokamaks. Due to the differences between conventional tokamaks and spherical tokamaks, it is not straightforward to transfer existing results about runaway dynamics in conventional tokamaks to STs. We have seen many similarities in the runaway generation to that in conventional tokamaks and in what follows, the results found when investigating the runaway dynamics in spherical tokamak disruptions, presented in Chapter 4, are summarised and related back to the questions raised in Chapter 1. Furthermore, some aspects that would be interesting to consider in future studies are highlighted.

5.1 Summary

The behaviour of unmitigated disruptions in ST reactors was studied in Section 4.1, assuming a thermal quench represented by an exponential temperature drop. The sensitivity of the current conversion to input parameters, including profile shape optimisation for energy confinement, was documented. We found that mitigation would typically be required to keep runaway current below acceptable levels, and that the runaway generation was comparable to that seen in conventional tokamak reactor scenarios.

Disruption mitigation by mixed deuterium and neon injection was then evaluated in Section 4.2. Whilst successful control of the ohmic current evolution and runaway currents seems to be within reach, the transported energy level is too high due to the peaked density and large temperature pedestal. We now revisit specifically the questions stated in the introduction.

In unmitigated disruptions, what are the respective contributions from different runaway generation mechanisms to the total runaway current? In all unmitigated disruptions modelled in Section 4.1, the dominant primary runaway generation mechanism was hot-tail. The overall dominant generation mechanism was avalanche multiplication, which is to be expected given its exponential increase with the plasma current and the high initial plasma current (21 MA). Generally, tritium decay was significantly larger than Dreicer generation of runaways, even though neither of them had any noticeable effect on the total runaway generation rate in the presence of hot-tail and avalanche, being lower than hot-tail by around 6 and 18 orders of magnitude, respectively.

What is the effect on runaway generation due to the evolution of the plasma shape throughout the disruption? In what way does including the effect of the compact ST *shape through so-called trapping corrections (e.g. including the effect of toroidicity on runaway growth rates) affect the runaway generation?* In Section 4.1.3 we showed that both removing the shaping, as well as removing the trapping corrections, increase the runaway current. When removing the shaping the increase was due to a higher electric field, while the increase when removing the trapping correction was due to more current contributing on larger flux surfaces. Therefore, if the plasma evolves during the disruption from its highly shaped initial state through to a smaller, more circular configuration as the outer layers of plasma are possibly lost during the disruption, we could imagine that the potential for runaway generation could increase compared to the results given here at constant shape.

Does the energy confinement optimisation of the BurST profiles impact the runaway generation? Yes, the optimisation for energy confinement also reduced the amount of runaways generated. Importantly, we found that the trends when varying parameters as in Section 4.1.3 were the same for un-optimised and optimised profiles, illustrating a robustness towards the input profiles in the results from the sensitivity study.

How do changes in relevant physical and structural parameters (e.g. temperature decay rate, wall time accounting for finite resistivity of the structures surrounding the plasma, distance between the plasma and the wall) affect the runaway generation? Increasing the wall distance or decreasing the wall time lead to an increased runaway current, as we illustrated with the results in Section 4.1.3. In both cases this increase was due to an increased energy reservoir, either from the vacuum between the plasma and the wall, or from the surrounding structures. The scans over the parameters of the thermal quench decay rate in Section 4.1.1, together with the fact that the setup variations in Section 4.1.3 only led to the runaway current staying the same or increasing (apart from the special case of fully disabling the hot-tail seed), indicate that mitigation strategies are necessary for spherical reactor-scale tokamaks in many of the possible disruption scenarios, just as for conventional tokamaks.

How do disruption mitigation strategies based on injecting a mixture of deuterium and neon affect the runaway dynamics? We explored mitigation of disruptions with both fast and slow thermal quenches in Section 4.2. It was found that similar mixtures of moderate amounts of neon and deuterium injection could be used in both of the studied cases to obtain a tolerable runaway current and current quench time simultaneously. However, this was also accompanied by a transported thermal energy loss fraction above 80 %, owing to the strong pedestal in the pre-disruption temperature and the peaked density profile. Hence, all three demands could not be fulfilled simultaneously with the input profiles in Figure 3.1.

5.2 Outlook

There are several aspects of this thesis that could be expanded on to move towards quantitative predictions of the runaway generation in ST-based fusion reactors. Importantly, the effect of vessel activation has previously been found to have a significant effect on runaway generation in conventional tokamaks due to Compton scattering. This was demonstrated for example by Vallhagen *et al.* (2020), in which adequate mitigation for ITER-like parameters could not be achieved with mixed material gas injection in the activated phase of operations. Such modelling required the spectrum of γ-photons emitted from the plasma-facing components. Given for ITER in (Martín-Solís, Loarte & Lehnen, 2017), this remains to be determined for alternative reactor designs. However, the runaway current in high-current devices is only a logarithmically weak function of the seed (Vallhagen *et al.*, 2020), so it might not have a major effect on the result, although it could have a significant impact if the hot-tail and Dreicer seeds would be lost through transport during the TQ.

We have studied here the two limiting cases where either the same shaping was kept throughout the disruption or a circular cross-section was assumed throughout. In reality, the plasma shape usually evolves from having the given pre-disruption geometry to a more circular cross-section at the end of the disruption, as discussed earlier. This means that the current conversion in reality is likely to be somewhere between the two cases that we have studied. DREAM does currently not allow for the time evolution of shaping parameters, but it may be possible to implement by letting the user prescribe time-dependent shaping parameters.

Regarding the material injection it could be interesting to study another impurity, such as argon. Using a heavier impurity might lead to more radiation and thus possibly reduce the high transported fraction of the thermal energy loss, but at the same time we expect that is has the potential to lead to a larger avalanche, due to the larger number of bound target electrons (Hesslow *et al.*, 2019*a*). Also, relaxing the assumption of a flat density profile for the injected material would improve the model, as in reality the material is injected at the wall and in most cases begins to ionise immediately (Svenningsson *et al.*, 2021). Additionally, SPI (shattered pellet injection) might be considered instead of the neutral gas injection modelled in Section 4.2 (uniformly distributed at $t = 0$), as SPI has the potential to reach and cool the centre of the plasma (Vallhagen *et al.*, 2022).

No transport effects have been taken into account for the unmitigated disruptions in order to evaluate the worst case scenario, and only heat transport has been taken into account for mitigated disruptions. Transport affects the magnitude of runaway current that is eventually able to hit the wall, as it influences how much of the runaway current is dissipated before this happens. Not including transport for example leads to the hot-tail seed likely being overestimated, as discussed in Section 4.1.2, so including reliable models for transport processes is an outstanding issue.

References

Breizman, B. N., Aleynikov, P., Hollmann, E. M. & Lehnen, M. 2019 "Physics of runaway electrons in tokamaks". *Nuclear Fusion* **59** (8), 083 001, doi: `10.1088/1741-4326/ab1822`

Chen, F. F. 2016 Introduction to Plasma Physics and Controlled Fusion. Springer Cham, doi: `10.1007/978-3-319-22309-4`

Connor, J. & Hastie, R. 1975 "Relativistic limitations on runaway electrons". *Nuclear Fusion* **15** (3), 415–424, doi: `10.1088/0029-5515/15/3/007`

De Clercq, G. 2016 "Nuclear fusion reactor ITER's construction accelerates as cost estimate swells". URL `https://www.reuters.com/article/us-france-nuclear-iter-idUSKCN1271BC`. Accessed: 2022-06-16

Dreicer, H. 1959 "Electron and ion runaway in a fully ionized gas. i". *Phys. Rev.* **115**, 238–249, doi: `10.1103/PhysRev.115.238`

Embréus, O., Stahl, A. & Fülöp, T. 2018 "On the relativistic large-angle electron collision operator for runaway avalanches in plasmas". *Journal of Plasma Physics* **84**, 905840 102, doi: `10.1017/S002237781700099X`

Freidberg, J. P. 2007 Plasma Physics and Fusion Energy. Cambridge University Press, doi: `10.1017/CBO9780511755705`

Fülöp, T., Helander, P., Vallhagen, O., Embreus, O., Hesslow, L., Svensson, P., Creely, A. J., Howard, N. T. & Rodriguez-Fernandez, P. 2020 "Effect of plasma elongation on current dynamics during tokamak disruptions". *Journal of Plasma Physics* **86** (1), 474860 101, doi: `10.1017/S002237782000001X`

Gerhardt, S., Menard, J. & the NSTX team 2009 "Characterization of the plasma current quench during disruptions in the national spherical torus experiment". *Nuclear Fusion* **49** (2), 025 005, doi: `10.1088/0029-5515/49/2/025005`

Helander, P., Smith, H., Fülöp, T. & Eriksson, L.-G. 2004 "Electron kinetics in a cooling plasma". *Physics of Plasmas* **11**, 5704–5709, doi: `10.1063/1.1812759`

Hender, T. 2021 Private communication

Hesslow, L., Embréus, O., Hoppe, M., DuBois, T. C., Papp, G., Rahm, M. & Fülöp, T. 2018*a* "Generalized collision operator for fast electrons interacting with partially ionized impurities". *Journal of Plasma Physics* **84**, 905840 605, doi: `10.1017/S0022377818001113`

Hesslow, L., Embréus, O., Wilkie, G. J., Papp, G. & Fülöp, T. 2018*b*

"Effect of partially ionized impurities and radiation on the effective critical electric field for runaway generation". *Plasma Physics and Controlled Fusion* **60**, 074 010, DOI: `10.1088/1361-6587/aac33e`

Hesslow, L., Embréus, O., Vallhagen, O. & Fülöp, T. 2019*a* "Influence of massive material injection on avalanche runaway generation during tokamak disruptions". *Nuclear Fusion* **59** (8), 084 004, DOI: `10.1088/1741-4326/ab26c2`

Hesslow, L., Unnerfelt, L., Vallhagen, O., Embreus, O., Hoppe, M., Papp, G. & Fülöp, T. 2019*b* "Evaluation of the Dreicer runaway generation rate in the presence of high-z impurities using a neural network". *Journal of Plasma Physics* **85** (6), 475850 601, DOI: `10.1017/S0022377819000874`

Hollmann, E. M., Aleynikov, P. B., Fülöp, T., Humphreys, D. A., Izzo, V. A., Lehnen, M., Lukash, V. E., Papp, G., Pautasso, G., Saint-Laurent, F. & Snipes, J. A. 2015 "Status of research toward the ITER disruption mitigation system". *Physics of Plasmas* **22** (2), 021 802, DOI: `10.1063/1.4901251`

Hoppe, M. 2021 "Runaway-electron model development and validation in tokamaks". Ph.D. thesis, Chalmers University of Technology, Gothenburg, Sweden

Hoppe, M., Embreus, O. & Fülöp, T. 2021 "DREAM: A fluid-kinetic framework for tokamak disruption runaway electron simulations". *Computer Physics Communications* **268**, 108 098, ISSN 0010-4655, DOI: `https://doi.org/10.1016/j.cpc.2021.108098`

Lehnen, M. & the ITER DMS task force 2021 "The ITER disruption mitigation system - design progress and design validation". `https://tsdw.pppl.gov/Talks/2021/Lehnen.pdf`. Presented at Theory and Simulation of Disruptions Workshop, PPPL

Lloyd, B. 2009 "Recent advances in ST research and prospects for new ST capabilities". In "2009 23rd IEEE/NPSS Symposium on Fusion Engineering", (1–6), DOI: `10.1109/FUSION.2009.5226531`

Martín-Solís, J., Loarte, A. & Lehnen, M. 2017 "Formation and termination of runaway beams in ITER disruptions". *Nuclear Fusion* **57** (6), 066 025, DOI: `10.1088/1741-4326/aa6939`

McDevitt, C. J. & Tang, X.-Z. 2019 "Runaway electron generation in axisymmetric tokamak geometry". *EPL (Europhysics Letters)* **127** (4), 45 001, DOI: `10.1209/0295-5075/127/45001`

Miller, R. L., Chu, M. S., Greene, J. M., Lin-Liu, Y. R. & Waltz, R. E. 1998 "Noncircular, finite aspect ratio, local equilibrium model". *Physics of Plasmas* **5** (4), 973–978, DOI: `10.1063/1.872666`

Patel, B. 2021 "Confinement physics for a steady state net electric burning spherical tokamak". Ph.D. thesis, University of York

Pusztai, I., Hoppe, M. & Vallhagen, O. 2022 "Runaway dynamics in disruptions with current relaxation". *Submitted to the Journal of Plasma Physics*. URL `https://arxiv.org/abs/2206.00904`

Rechester, A. B. & Rosenbluth, M. N. 1978 "Electron heat transport in a tokamak with destroyed magnetic surfaces". *Phys. Rev. Lett.* **40**, 38–41, DOI: `10.1103/PhysRevLett.40.38`

Redl, A., Angioni, C., Belli, E. & Sauter, O. 2021 “A new set of analytical formulae for the computation of the bootstrap current and the neoclassical conductivity in tokamaks”. *Physics of Plasmas* **28** (2), 022 502, DOI: `10.1063/5.0012664`

Rosenbluth, M. & Putvinski, S. 1997 “Theory for avalanche of runaway electrons in tokamaks”. *Nuclear Fusion* **37** (10), 1355–1362, DOI: `10.1088/0029-5515/37/10/i03`

Smith, H., Helander, P., Eriksson, L.-G. & Fülöp, T. 2005 “Runaway electron generation in a cooling plasma”. *Physics of Plasmas* **12**, 122 505, DOI: `10.1063/1.2148966`

Sommariva, C., Nardon, E., Beyer, P., Hoelzl, M. & and, G. H. 2018 “Electron acceleration in a JET disruption simulation”. *Nuclear Fusion* **58** (10), 106 022, DOI: `10.1088/1741-4326/aad47d`

Svenningsson, I. 2020 “Hot-tail runaway electron generation in cooling fusion plasmas”. Master’s thesis, Chalmers University of Technology. URL `https://hdl.handle.net/20.500.12380/300899`

Svenningsson, I., Embreus, O., Hoppe, M., Newton, S. L. & Fülöp, T. 2021 “Hot-tail runaway seed landscape during the thermal quench in tokamaks”. *Physical Review Letters* **127**, 035 001, DOI: `10.1103/PhysRevLett.127.035001`

Svensson, P., Embreus, O., Newton, S. L., Särkimäki, K., Vallhagen, O. & Fülöp, T. 2021 “Effects of magnetic perturbations and radiation on the runaway avalanche”. *Journal of Plasma Physics* **87**, 905870 207, DOI: `10.1017/S0022377820001592`

Thornton, A. 2011 “The impact of transient mitigation schemes on the MAST edge plasma”. Ph.D. thesis, University of York

UKAEA 2022 “STEP”. URL `https://ccfe.ukaea.uk/research/step/`. Accessed: 2022-06-16

Vallhagen, O., Embreus, O., Pusztai, I., Hesslow, L. & Fülöp, T. 2020 “Runaway dynamics in the DT phase of ITER operations in the presence of massive material injection”. *Journal of Plasma Physics* **86** (4), 475860 401, DOI: `10.1017/S0022377820000859`

Vallhagen, O., Pusztai, I., Hoppe, M., Newton, S. L. & Fülöp, T. 2022 “Effect of two-stage shattered pellet injection on tokamak disruptions”. *Nuclear Fusion* URL `https://iopscience.iop.org/article/10.1088/1741-4326/ac667e`

Wesson, J. & Campbell, D. 2004 Tokamaks. International series of monographs on physics, 3rd edn., Oxford University Press, ISBN 9780198509226

Wilson, H., Ahn, J.-W., Akers, R., Applegate, D., Cairns, R., Christiansen, J., Connor, J., Counsell, G., Dnestrovskij, A., Dorland, W., Hole, M., Joiner, N., Kirk, A., Knight, P., Lashmore-Davies, C., McClements, K., McGregor, D., O'Brien, M., Roach, C., Tsaun, S. & Voss, G. 2004 “Integrated plasma physics modelling for the culham steady state spherical tokamak fusion power plant". *Nuclear Fusion* **44** (8), 917–929, DOI: `10.1088/0029-5515/44/8/010`

A

Shaping Parameters

The flux surfaces of the unmodified equilibrium are shown in Figure A.1b. From Section 3.1 we know that flux surfaces in DREAM are parameterised by shaping parameters, $\kappa(r)$, $\Delta(r)$, $\delta(r)$, $\psi_{\mathrm{ref}}(r)$, and $G(r)$. As explained in Section 3.2, the shaping profiles parameterising the flux surfaces of the unmodified equilibrium are not compatible with DREAM and thus needed to be modified.

First, we noted that the extracted shaping profiles were not completely smooth, as they were numerically calculated from the equilibrium in Figure A.1b. As the poloidal magnetic field strength depends on radial derivatives of the shaping profiles, the non-smoothness caused B_θ to vary significantly. This issue was solved by fitting polynomials to the shaping profiles. Further, the magnitude of the Shafranov shift $\Delta(r)$ at large r gives rise to double magnetic field strength minima on the outer flux surfaces. From Figure A.1a we see that the original Δ-profile (dotted curve) was about $-0.5\,\mathrm{m}$ at the edge and we have empirically found that limiting the edge value of the Shafranov shift to $-0.3\,\mathrm{m}$ is sufficient to avoid the issue of double minima. We have considered two simple approaches to accomplish this; either to multiply the entire Shafranov shift profile with a factor smaller than 1, or to modify the slope of the profile for large r, to obtain $\Delta(r=a) \approx -0.3\,\mathrm{m}$. As can be seen in Figure A.1a (solid curve) we chose the second option, as this solution only modifies the profile for a limited r-range, whereas the first option would modify the profile over almost the entire r-range. The entire profile was also shifted so that $\Delta(r = 0\,\mathrm{m}) = 0\,\mathrm{m}$, as this is in accordance with the definition of the Shafranov shift in DREAM.

The resulting equilibrium, parameterised by the modified shaping profile, is shown in Figure 3.1d. This has been used throughout all simulations in this thesis, except for the un-optimised case, where the same modifications were applied to its similar corresponding equilibrium.

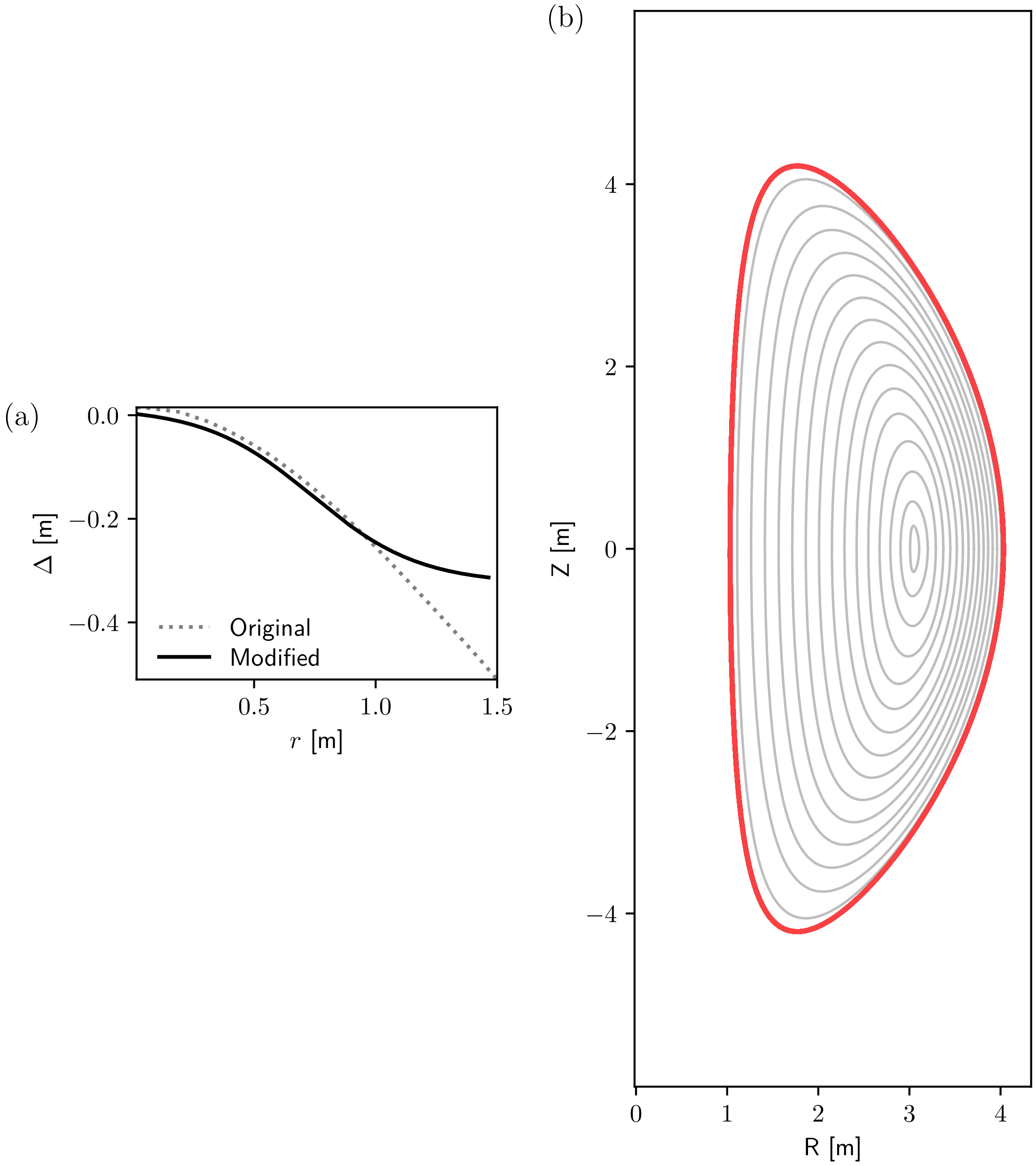

Figure A.1: (a) Radial profiles for the original and modified Shafranov shifts and (b) shape of the unmodified equilibrium flux surfaces.

DEPARTMENT OF PHYSICS
CHALMERS UNIVERSITY OF TECHNOLOGY
Gothenburg, Sweden
www.chalmers.se